

Shear viscosity from perturbative Quantum Chromodynamics to the hadron resonance gas at finite baryon, strangeness, and electric charge densities

Isabella Danhoni,^{1,*} Jordi Salinas San Martín,² and Jacquelyn Noronha-Hostler²

¹*Institut für Kernphysik, T. U. Darmstadt,*

Schlossgartenstraße 2, D-64289 Darmstadt, Germany

²*Illinois Center for Advanced Studies of the Universe, Department of Physics,*

University of Illinois at Urbana-Champaign, Urbana, IL 61801, USA

Abstract

Through model-to-data comparisons from heavy-ion collisions, it has been shown that the Quark Gluon Plasma has an extremely small shear viscosity at vanishing densities. At large baryon densities, significantly less is known about the nature of the shear viscosity from Quantum Chromodynamics (QCD). Within heavy-ion collisions, there are three conserved charges: baryon number (B), strangeness (S), and electric charge (Q). Here we calculate the shear viscosity in two limits using perturbative QCD and an excluded-volume hadron resonance gas at finite BSQ densities. We then develop a framework that interpolates between these two limits such that shear viscosity is possible to calculate across a wide range of finite BSQ densities. We find that the pQCD and hadron resonance gas calculations have different BSQ densities dependence such that a rather non-trivial shear viscosity appears at finite densities.

* idadhoni@theorie.ikp.physik.tu-darmstadt.de

CONTENTS

I. Introduction	2
II. Calculation of shear viscosity at finite temperatures and densities	5
A. Thermodynamics	5
B. Perturbative QCD	7
C. Hadron Resonance Gas Model with an Excluded-Volume	11
D. Switching between models	15
III. Building a phenomenological model of three conserved charges	18
IV. Results for $\eta T/w$	22
A. $\eta T/w$ at finite μ_B and overall magnitude	22
V. $\eta T/w$ in the presence of three conserved charges	27
A. Fixing $\eta T/w$ at the transition points	30
VI. Conclusions and Outlook	33
Acknowledgments	34
References	35

I. INTRODUCTION

The Quark Gluon Plasma (QGP) produced in heavy-ion collisions at the Relativistic Heavy-Ion Collider (RHIC) or Large Hadron Collider (LHC) is a deconfined state of matter composed of quarks and gluons [1–4]. Around the phase transition between quarks and gluons into hadrons, the matter is very strongly-interacting and has been shown to have an extremely small shear viscosity to entropy density ratio (η/s) that reaches approximately the so-called KSS limit [5]. State-of-the-art Bayesian analyses [6–9] using relativistic viscous hydrodynamics estimate the value of η/s in this regime to be approximately $\eta/s \sim 0.08$ – 0.2 , when considering the regime of vanishing baryon density. It is generally believed that there is a minimum in η/s [10] in the strongly-interacting regime around the cross-over

phase transition between quarks and gluons into hadrons and that η/s then increases as the interactions become weaker either at high temperatures in the quark phase [11–14] or low temperatures in the Hadron Resonance Gas (HRG) phase [15–29]. However, the functional form of η/s at vanishing densities is hard to discern from data and may still yet be consistent with $\eta/s \sim \text{const}$. One should also note that the Bayesian analyses use functional forms of η/s , not microscopic calculations and, therefore, it is not possible to easily extrapolate these results to new, yet under-explored regions of the Quantum Chromodynamics (QCD) phase diagram.

It is not yet possible to directly calculate η/s in the strongly-interacting regime directly from lattice QCD due to the Fermion-sign problem [30, 31] (although this may eventually be possible with quantum computers [32]). Instead one can calculate shear viscosity in the weakly coupled regime using perturbative QCD (pQCD) calculations as has been done previously at vanishing baryon densities [11–14] and for the first time, recently at finite baryon densities [33]. These pQCD calculations are most applicable at high temperatures where one expects the QGP to become weakly coupled. Although the exact temperature T where pQCD calculations are applicable is still ambiguous, at low temperatures it is possible to calculate the shear viscosity using the known properties of the HRG using kinetic theory. For instance, one can use an HRG with an excluded-volume [34–36] that decreases with increasing temperature—the behavior one anticipates if there is a minimum of η/s at the cross-over phase transition. This behavior of η/s in the HRG can be understood because more degrees of freedom open up at higher T , which increases the entropy and therefore lowers η/s [15]. However, HRG calculations using the latest Particle Data Group (PDG) hadronic list as of 2016 with over 700 hadrons in it, found the value of η/s to be significantly larger than anticipated from Bayesian analyses [36]. An alternative approach to HRG models but within the same regime are the calculations from hadron transport theory [16, 27, 37], although one would want to include the latest PDG list (see [38]), which remains for a future work. Within the strongly coupled regime a popular approach has been holography wherein a “fuzzy” lower bound of $\eta/s = 1/(4\pi)$ has been calculated known as the KSS limit [5]. However, there are various ways in holography to introduce a T dependence in η/s [39] or break this bound [40–43]. Alternatively, a variety of non-perturbative techniques for quantum field theories have been developed to calculate η/s as well [44, 45].

Up until this point, we have we have only discussed the behavior of shear viscosity at

vanishing densities, i.e., the regime applicable at top LHC energies. For finite densities (n_B), η/s is no longer the correct quantity of interest but rather one uses $\eta T/w$ where $w = \varepsilon + p$ is the enthalpy (for vanishing baryon densities the two quantities become identical), ε is the energy density, and p is the pressure. The search is currently underway for the QCD critical point at large baryon densities [46–49] and rich physics questions open up in this regime that relate to shear viscosity. However, at large baryon densities little is known about the behavior of shear viscosity and various model calculations have shown either an increase [50] or decrease [51, 52] in $\eta T/w$ as the baryon chemical potential μ_B increases. Preliminary Bayesian analyses suggest that $\eta T/w$ should increase with μ_B [53, 54] but no clear functional form has been extracted from data yet. The presence of a critical point/first-order phase transition at large μ_B would also influence the behavior of $\eta T/w$. While the influence of any critical scaling is most likely negligible for the shear viscosity [55], the location of the critical point can affect the finite μ_B behavior because all inflection points must converge at the critical point (i.e., the minimum of $\eta T/w$), see [36, 52] for more details. After the critical point one anticipates a jump in $\eta T/w$ across the first-order phase transition line [50, 52].

To summarize, we can expect certain behaviors of $\eta T/w$ if there is a critical point. However, the location and even the existence of the QCD critical point is still quite uncertain. Thus, we require a framework to describe $\eta T/w$ at finite μ_B that can shift the location of the critical point or have no critical point whatsoever. To achieve this, we must incorporate the required features and phase transitions as described above, while allowing for flexibility in when and how these changes occur between phases.

A further complication is that at large baryon densities other globally conserved charges play a significant role. For instance, due to strangeness neutrality and the existence of strange baryons and mesons in the QGP, one acquires a rather large strangeness chemical potential at finite μ_B . In fact, $\mu_S \sim \mu_B/3$ when one enforces strangeness neutrality. Additionally, electric charge also plays a role since the nuclei that are stopped contain a large number of protons that carry electric charge. The ratio of the number of protons Z to the total number of nucleons A in the nuclei remains fixed globally throughout the lifetime of the QGP such that $Z/A = \text{const}$. For heavy nuclei used in relativistic heavy-ion collisions the values range from $Z/A \sim 0.38$ – 0.45 . Enforcing conservation of electric charge leads to a small, negative μ_Q that is approximately one tenth of μ_B in magnitude, i.e., $\mu_Q \sim -\mu_B/10$ [56]. Thus far, we have only discussed the global values of the chemical potentials, but it

is also possible to have local fluctuations of conserved charges (as long as the strangeness neutrality and electric charge conservation are enforced globally); see examples [57–59]. In those cases, you actually require an equation of state that is 4-dimensional such that it depends on temperature, baryon (B) chemical potential, strangeness (S) chemical potential, and electric charge (Q) chemical potential: $\{T, \mu_B, \mu_S, \mu_Q\}$ and must also have a description for $\eta T/w(T, \mu_B, \mu_S, \mu_Q)$. Currently, no such description exists.

In this work, we first calculate $\eta T/w(T, \mu_B, \mu_S, \mu_Q)$ in two limits: pQCD with 3 flavors and HRG with an excluded-volume. Then we use various functional forms to interpolate between these two limits. We use comparisons to lattice QCD to motivate the points of switching between the HRG to an intermediate regime and from this to pQCD. Additionally, we renormalize the magnitude of $\eta T/w$ at vanishing densities to reproduce the values of shear viscosity extracted from Bayesian analyses, similar to what was done in previous work [36]. Finally, we demonstrate the non-trivial behavior of $\eta T/w(T, \mu_B, \mu_S, \mu_Q)$ that appears in our framework.

II. CALCULATION OF SHEAR VISCOSITY AT FINITE TEMPERATURES AND DENSITIES

In this section we will cover the calculations of shear viscosity both at high temperatures within pQCD calculations but also at low temperatures within HRG calculations. Before doing so, though, we will review some basic thermodynamic relations for an ideal, relativistic gas of non-interacting particles with multiple conserved charges since this is relevant for both our high and low T studies.

A. Thermodynamics

We begin this section by presenting the thermodynamics of an ideal, relativistic gas of point-like particles, which will be used for the weakly interacting QCD and the hadron resonance gas phases. Later on in Sec. II C we will also discuss the possibility of excluded-volume effects that act as repulsive interactions. In the grand canonical ensemble formulation, the ideal gas reduces to an uncorrelated gas of free particles [60]. For such a system, we can

write the partition function as

$$T \ln Z_{\text{id}} = \sum_i \frac{g_i V}{6\pi^2} \int_0^\infty \frac{dk k^4}{\sqrt{k^2 + m_i^2}} \frac{1}{\exp \left[(\sqrt{k^2 + m_i^2})/T - \tilde{\mu}_i \right] + (-1)^{B_i-1}}, \quad (1)$$

where $\tilde{\mu}$ is the effective chemical potential for each particle, i , defined as

$$\tilde{\mu}_i = B_i \frac{\mu_B}{T} + S_i \frac{\mu_S}{T} + Q_i \frac{\mu_Q}{T}, \quad (2)$$

and the spin degeneracy $g_i = 2J_i + 1$ of each hadron with spin J_i , m_i is the mass, and B_i is the baryon number, S_i is strangeness, and Q_i is the electric charge. Additionally, μ_B , μ_S , and μ_Q are the corresponding chemical potentials for each conserved charge.

Consider now a free gas of u , d , and s flavors that, through their respective quantum numbers, lead to BSQ conserved charges. From this, one can derive the partition function for a massless gas of fermions and bosons,

$$T \ln Z_{\text{QGP}} = \frac{g_g V}{90\pi^2} T^4 + \sum_i \frac{g_f V}{12} \left(\frac{7\pi^2}{30} T^4 + \tilde{\mu}_i^2 T^2 + \frac{1}{2\pi^2} \tilde{\mu}_i^4 \right). \quad (3)$$

Here, $g_g = 16$ accounts for the gluon degrees of freedom, since the gluon has 8 colors and two helicities. The factor $g_f = 6$ accounts for 2 helicities and 3 colors for the quarks, and the sum is over quark flavors. The contribution from anti-quarks is already included in the partition function and does not require extra counting.

From the partition function, one can calculate the thermodynamic properties of the system such as the pressure p , the energy density ε , and the n number density:

$$p(T, \mu_B, \mu_S, \mu_Q) = \frac{T \ln Z}{V}, \quad (4)$$

$$\varepsilon(T, \mu_B, \mu_S, \mu_Q) = \frac{T^2}{V} \frac{\partial \ln Z}{\partial T} + \tilde{\mu} n(T, \mu_B, \mu_S, \mu_Q), \quad (5)$$

$$n(T, \mu_B, \mu_S, \mu_Q) = \frac{T}{V} \frac{\partial \ln Z}{\partial \tilde{\mu}}. \quad (6)$$

Using these relations, we can calculate other thermodynamic quantities:

$$s(T, \mu_B, \mu_S, \mu_Q) = \frac{\partial p(T, \mu_B, \mu_S, \mu_Q)}{\partial T}, \quad (7)$$

$$\frac{\rho_X(T, \mu_B, \mu_S, \mu_Q)}{T^3} = \frac{\partial p(T, \mu_B, \mu_S, \mu_Q)/T^4}{\partial(\mu_X/T)}, \quad (8)$$

where s is the entropy density and ρ_X is the net density associated with a specific conserved charge $X = B, S, Q$. All of these thermodynamic quantities can be connected through the Gibbs-Duhem relation,

$$\varepsilon + p = sT + \sum_{X=B,S,Q} \mu_X \rho_X. \quad (9)$$

B. Perturbative QCD

Transport coefficients of a weakly coupled QCD medium can be obtained using a kinetic theory description. This was first done correctly by Arnold, Moore and Yaffe [11, 12], and later expanded by Danhoni and Moore [33] to the high-density region. In this work, we use the results found for shear viscosity calculations as a function of μ_B and use the same formalism to derive η for finite μ_Q , μ_S as well. Therefore, we briefly revise the important aspects of this calculation and discuss the differences for this specific case.

As mentioned before, these calculations are based on the kinetic theory description of the hot dense QCD in a weakly coupled regime. In this description, shear viscosity is a property relevant for systems with space-nonuniform flow velocity, meaning that the local equilibrium form of the statistical function is given by the Fermi-Dirac and Bose-Einstein distributions:

$$f_0^{q/\bar{q}} = \frac{1}{\exp(\beta p - \tilde{\mu}) + 1}, \quad f_0^g = \frac{1}{\exp(\beta p) - 1}. \quad (10)$$

Here $\beta^{-1} = T$ is the local temperature. In order to describe a generic state that is not necessarily in equilibrium we then require a distribution that includes both the equilibrium f_0^a and out-of-equilibrium contributions f_1^a . This system has a non-equilibrium distribution that is given by:

$$f^a(\vec{k}, \vec{x}) = f_0^a(\vec{k}, \vec{x}) + f_0^a(1 \pm f_0^a) f_1^a(\vec{k}, \vec{x}), \quad (11)$$

in which a represents the species considered (a gluon, quark, or anti-quark) and the dynamics of the non-equilibrium distribution f^a are determined from a Boltzmann-type equation, where time derivatives and external forces are not relevant. Thus, we can simply write it as

$$\vec{v}_k \cdot \frac{\partial}{\partial \vec{x}} f^a(\vec{k}, \vec{x}, t) = -\mathcal{C}^a[f]. \quad (12)$$

Note that we neglect thermal and Lagrangian masses, making the velocity vector the unit vector in the direction of the momentum, $\vec{v}_p = \hat{p} \equiv \vec{p}/p$, and only consider first-order contributions to the collision operator. This leads to

$$\begin{aligned} \mathcal{C}^a[f](\vec{p}) &= \frac{1}{2} \sum_{bcd} \int_{\vec{k}, \vec{p}, \vec{k}'} \frac{|\mathcal{M}_{abcd}(P, K, P', K')|^2}{2p^0 2k^0 2p'^0 2k'^0} (2\pi)^4 \delta^4(P + K - P' - K') \\ &\quad \times \left\{ f^a(\vec{p}) f^b(\vec{k}) [1 \pm f^c(\vec{p}')][1 \pm f^d(\vec{k}')] \right. \\ &\quad \left. - f^c(\vec{p}') f^d(\vec{k}') [1 \pm f^a(\vec{p})][1 \pm f^b(\vec{k})] \right\}, \quad (13) \end{aligned}$$

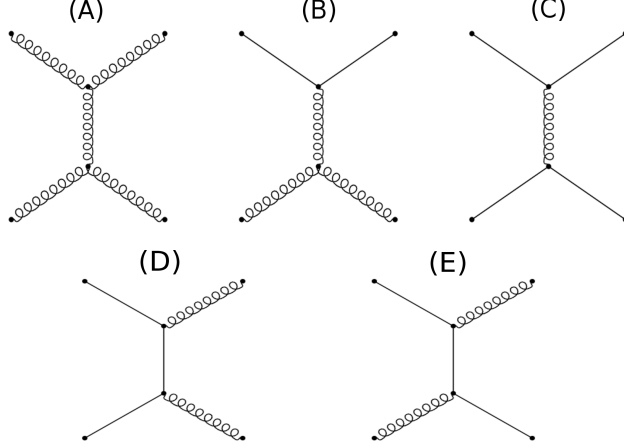


FIG. 1. Feynman diagrams of the scattering contributing at leading logarithmic order [33].

where \mathcal{M} represents the scattering matrix of the processes of interest, calculated using perturbative QCD; the relevant diagrams for shear viscosity at leading logarithmic order are shown in Fig. 1. The sum in Eq. (13) is over all scattering processes in the QGP of type $a + b \rightarrow c + d$. A detailed description of how to compute the contribution pertaining to each diagram and how to use the variational method to obtain shear viscosity can be found in [33]. The procedure can be extended for the case of multiple chemical potentials with some minor differences. As a consequence of having multiple charges, different flavors of quarks and anti-quarks must have different relaxation functions,

$$\begin{aligned}
 \chi^u(k) &= \sum_{m=1}^N a_{m+N} \phi^{(m)}(k), & \chi^d(k) &= \sum_{m=1}^N a_{m+2N} \phi^{(m)}(k), & \chi^s(k) &= \sum_{m=1}^N a_{m+3N} \phi^{(m)}(k), \\
 \chi^{\bar{u}}(k) &= \sum_{m=1}^N a_{m+4N} \phi^{(m)}(k), & \chi^{\bar{d}}(k) &= \sum_{m=1}^N a_{m+5N} \phi^{(m)}(k), & \chi^{\bar{s}}(k) &= \sum_{m=1}^N a_{m+6N} \phi^{(m)}(k), \\
 \chi^g(k) &= \sum_{m=1}^N a_m \phi^{(m)}(k),
 \end{aligned} \tag{14}$$

where a_m is a variational parameter, and N is the size of the basis set one uses to solve the Boltzmann equation. In this paper, the basis set used for it was the same as used in [33]:

$$\phi^{(m)}(k) = \frac{k(k/T)^m}{(1 + k/T)^{N-1}}, \quad m = 1, \dots, N. \tag{15}$$

This change implies that the contribution from each quark in all diagrams has to be counted separately; therefore, the scattering matrix will evolve differently as a function of each chem-

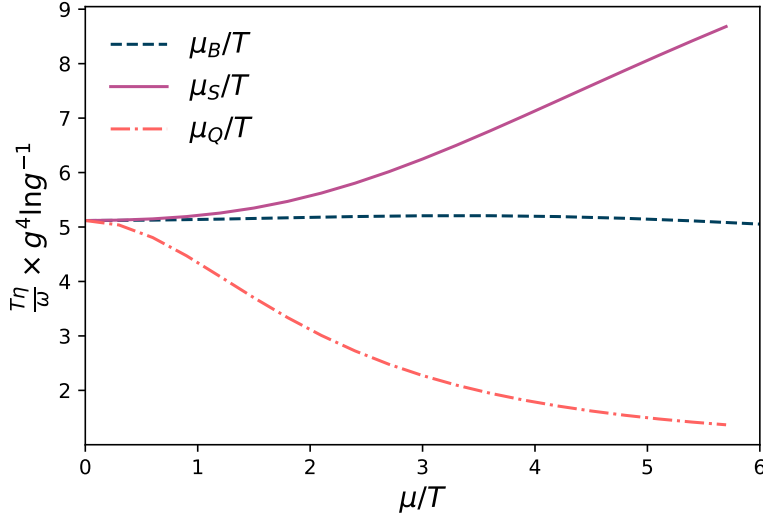


FIG. 2. (color online) $\eta T/w$ at finite charge chemical potentials as a function of μ_B/T (dashed blue), μ_S/T (solid purple), and μ_Q/T (dot-dashed red) from pQCD. Every contribution is calculated while fixing the other chemical potentials to zero.

ical potential. As discussed previously, at finite densities, the shear viscosity is normalized by T/w such that we require knowledge of the enthalpy, i.e., $w = \varepsilon + p$.

Figure 2 shows a curve for $\eta T/w$ as a function of μ_B/T , μ_S/T , and μ_Q/T while having the other chemical potentials are set to zero. The curves exhibit completely different behaviors, suggesting that shear viscosity is strongly dependent on which chemical potential is present in the system. We find that $\eta T/w$ increases with increasing μ_S whereas $\eta T/w$ decreases with decreasing μ_Q . Previous work on finite μ_B only found that $\eta T/w$ increased slightly before generally decreasing at $\mu_B/T \gtrsim 1$ [33]. Note that the values of μ_S and μ_Q here are chosen to be positive but the results should have reflection symmetry in μ when only one chemical potential is finite. Thus, all three chemical potentials on their own lead to strikingly different behaviors. These differences can be explained by the fact that ρ_Q grows slower as a function of μ_Q than what would happen for ρ_B and ρ_S , and this affects the enthalpy, which will change significantly less than for the same value of μ_B or μ_S .

In order to understand the interplay between chemical potentials, we next hold $\mu_Q = 0$ fixed and vary μ_B and μ_S . In Fig. 3 (left) we plot μ_B/T on the x -axis while varying μ_S/T using different colors (shown in the color bar to the right of the plot). Also, in Fig. 3 (right) we vary μ_S/T on the x -axis while varying μ_B/T using different colors. When varying μ_B/T

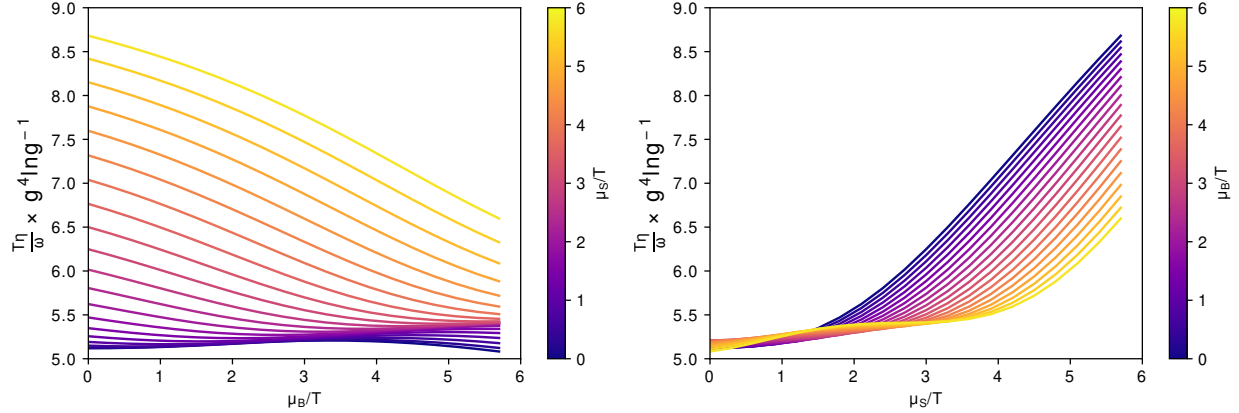


FIG. 3. (color online) Behavior of $\eta T/w$ as a function of (left) μ_B for varying μ_S and (right) μ_S for varying μ_B for the pQCD calculations performed here. In both cases, $\mu_Q = 0$.

on the x -axis, we find that the overall $\eta T/w$ can have a variety of qualitative behaviors across $\eta T/w$. For instance, $\eta T/w$ may increase then decrease, decrease then increase, or decrease only—all depending on what is the corresponding value of μ_S/T . In general, though, increasing the value of μ_S/T leads to an overall increase in the magnitude of $\eta T/w$. On the other hand, in the case of varying μ_S/T on the x -axis, the qualitative behavior of $\eta T/w$ is not as strongly affected by different values of μ_B/T , showing a monotonic increase in $\eta T/w$ for the chemical potential ranges considered. However, we do find that a smaller μ_B/T ratio leads to a larger overall increase in $\eta T/w$ at large μ_S/T , whereas a larger μ_B/T ratio tends to dampen the step rise in $\eta T/w$ at large μ_S/T . Generally, we expect that systems that have large μ_B also have a reasonably large μ_S such that we anticipate a modification of $\eta T/w$ due to the effects of strangeness.

To get a better understanding of what is probed in heavy-ion collision experiments, we explore the “strangeness neutral” (SN) case where the two following conditions are enforced:

$$\langle \rho_Q \rangle = \frac{Z}{A} \langle \rho_B \rangle, \quad (16)$$

$$\langle \rho_S \rangle = 0, \quad (17)$$

where the first constraint comes from the conservation of electric charge and the second comes from strangeness neutrality. In principle, we have 4 degrees of freedom $\{T, \mu_B, \mu_S, \mu_Q\}$ but for the strangeness neutral trajectories through the QCD phase diagram then $\mu_S(T, \mu_B)$ and $\mu_Q(T, \mu_B)$ are constrained to be single values for a specific temperature and baryon chemical potential. In Fig. 4, we compare $\eta T/w$ for the case of only finite μ_B (pink) compared

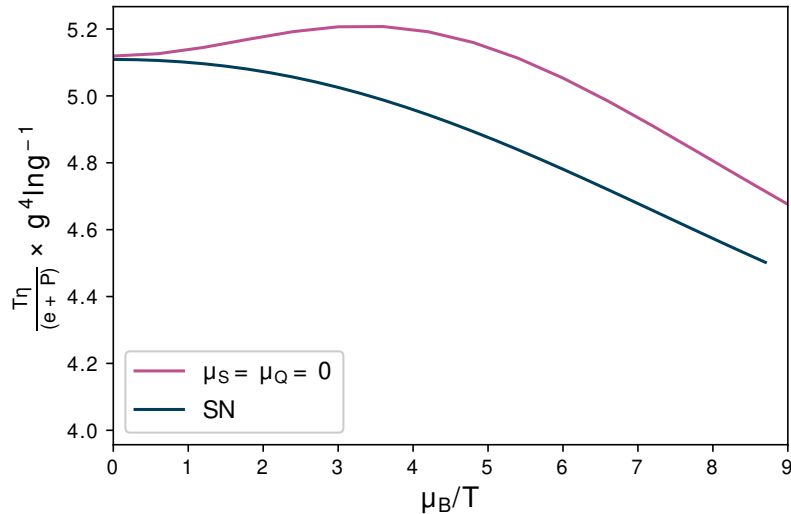


FIG. 4. (color online) Shear viscosity as a function of $\mu_S(T, \mu_B)$ and $\mu_Q(T, \mu_B)$ for (black) the strangeness neutral case that has the conditions shown in Eqs. (16) and (17) compared to (pink) the case of $\mu_S = \mu_Q = 0$.

to the strangeness neutral trajectory (black) where we set $Z/A = 0.4$. For finite μ_B , there is a non-monotonic behavior in $\eta T/w$. However, once we enforce the strangeness neutrality conditions, we find that the non-monotonicity disappears and $\eta T/w$ only decreases with increases μ_B . The effect of the strangeness neutral case is consistent with Fig. 3 (left) wherein if we have both finite μ_B and a sufficiently large μ_S we find that the effect of μ_S can lead to a monotonically decreasing $\eta T/w$.

C. Hadron Resonance Gas Model with an Excluded-Volume

At low temperatures in heavy-ion collisions, the QGP freezes-out into a gas of interacting hadrons. In this regime, we can use the hadron resonance gas model, where we include repulsive interactions through an excluded-volume (EV-HRG) such that the hard-core volume is

$$v = 4 \cdot \frac{4}{3} \pi r^3, \quad (18)$$

where r is the radius of an individual hadron. The factor of 4 is because the excluded-volume for a sphere is 8 times its volume, but this is shared across two interacting particles, hence a factor of 4. Here we make the simple assumption that all hadrons have the same volume,

but it is possible to relax this assumption (see, for example, Ref. [61]).

Before including the excluded-volume, we begin with the ideal hadron resonance gas model where the equation of state is described using a gas of free hadrons (see Sec. II A). With this model, one can obtain thermodynamic quantities and transport coefficients assuming that hadrons are point-like particles. The total density of particles for species i can be calculated from the partition function such that

$$\frac{n_i^{\text{id}}(T, \mu_B, \mu_S, \mu_Q)}{T^3} = \frac{g_i}{2\pi^2} \int_0^\infty dk k^2 \left[\exp\left(\frac{\sqrt{k^2 + m_i^2}}{T} - \tilde{\mu}_i\right) + (-1)^{B_i-1} \right]^{-1}, \quad (19)$$

where B_i is the baryon number of the particle, k is the momentum, m_i is the mass of the particle, and the degeneracy factor $g_i = 2J_i + 1$ comes from spin J_i . The effective chemical potential for species i is defined in the same way as above in Eq. (2).

Next, we include repulsive interactions through an excluded-volume. The excluded-volume pressure is given by the self-consistent equation

$$\frac{p^{\text{ex}}(T, \mu_B, \mu_S, \mu_Q)}{T} = n^{\text{id}}(T, \mu_B, \mu_S, \mu_Q) \exp\left(\frac{-v p^{\text{ex}}(T, \mu_B, \mu_S, \mu_Q)}{T}\right), \quad (20)$$

where p^{ex} is our excluded-volume pressure. If all hadrons have the same v , this self-consistent equation can be solved analytically using the Lambert W function,

$$p^{\text{ex}}(T, \mu_B, \mu_S, \mu_Q) = \frac{T}{v} W(v n^{\text{id}}(T, \mu_B, \mu_S, \mu_Q)). \quad (21)$$

Here, $n^{\text{id}}(T, \mu_B, \mu_S, \mu_Q)$ is the number density defined in Eq. (19). The remaining thermodynamic quantities can be derived using the relationships in Sec. II A (we specifically require the enthalpy w to normalize the shear viscosity). We consider that all particles have the same volume, such that in the limit $v \rightarrow 0$, one should recover the ideal gas description [35, 36]. The calculations for the thermodynamic variables were performed using the THERMAL-FIST package [62] with the PDG2021+ particle list [38].

Now, we can discuss the calculations of the shear viscosity. In kinetic theory, the shear viscosity is proportional to

$$\eta \propto n_{\text{tot}} \sum_i \lambda_i \langle |k| \rangle_i, \quad (22)$$

where n_{tot} is the total particle number density defined as

$$n_{\text{tot}} = \sum_i n_i, \quad (23)$$

where λ_i is the mean free path such that $\lambda \propto 1/(n_i r^2)$ and $\langle |k| \rangle_i$ is the average thermal momentum of particle i . We emphasize here that the total particle number density n_{tot} here is not the same as the net-baryon density ρ_B . Rather, to calculate the baryon density, we would need to include a weight for each particle species according to its baryon number (e.g., for (anti)protons $B_p = 1$ and $B_{\bar{p}} = -1$) such that at vanishing chemical potentials, $\rho_B = 0$. Since we know that η does not vanish at vanishing $\tilde{\mu} = 0$, instead what enters is the sum of all particles and anti-particles without a weight with the baryon density (such that mesons are also included). Thus, the total particle density elucidates the amount total matter plus anti-matter in the system, not the net amount of matter.

In the hadron resonance gas model, we can describe the average thermal momentum as:

$$\langle |k| \rangle_i = \frac{\int_0^\infty k^3 \exp \left[-\sqrt{k^2 + m_i^2}/T + \tilde{\mu}_i \right] dk}{\int_0^\infty k^2 \exp \left[-\sqrt{k^2 + m_i^2}/T + \tilde{\mu}_i \right] dk}, \quad (24)$$

which is just the integral weighted by momentum. However, because the $\tilde{\mu}_i$ term is independent of the momentum, we can pull it out of the integral such that it cancels out and Eq. (24) simplifies to

$$\langle |k| \rangle_i = \frac{\int_0^\infty k^3 \exp \left[-\sqrt{k^2 + m_i^2}/T \right] dk}{\int_0^\infty k^2 \exp \left[-\sqrt{k^2 + m_i^2}/T \right] dk} \quad (25)$$

even at finite chemical potentials. Substituting this into Eq. (22), we obtain

$$\eta \propto \frac{1}{r^2} \sum_i \frac{n_i \int_0^\infty k^3 \exp \left[-\sqrt{k^2 + m_i^2}/T \right] dk}{n \int_0^\infty k^2 \exp \left[-\sqrt{k^2 + m_i^2}/T \right] dk} \quad (26)$$

if we continue to assume a single hard-core radius for all hadrons (otherwise r would remain inside of the summation). Next, we focus specifically on the particle number density n_i . For an ideal gas the particle number density is shown in Eq. (19) for species i . When including the excluded-volume effects, we can then write

$$n_i^{\text{ex}} = \frac{e^{-vp^{\text{ex}}/T} n_i^{\text{id}}}{1 + v e^{-vp^{\text{ex}}/T} n_{\text{tot}}^{\text{id}}}, \quad (27)$$

where the total excluded-volume particle number density is

$$\begin{aligned} n_{\text{tot}}^{\text{ex}} &= \sum_i n_i^{\text{ex}} \\ &= \sum_i \frac{e^{-vp^{\text{ex}}/T} n_i^{\text{id}}}{1 + v e^{-vp^{\text{ex}}/T} n_{\text{tot}}^{\text{id}}} \end{aligned} \quad (28)$$

and assuming still that the excluded-volume v is the same for all particle species then we pull out the n_i^{id} term from the summation such that

$$n_{\text{tot}}^{\text{ex}} = n_{\text{tot}}^{\text{id}} \frac{e^{-vp^{\text{ex}}/T}}{1 + ve^{-vp^{\text{ex}}/T} n_{\text{tot}}^{\text{id}}}. \quad (29)$$

Therefore, the ratios

$$\frac{n_i^{\text{ex}}}{n_{\text{tot}}^{\text{ex}}} = \frac{n_i^{\text{id}}}{n_{\text{tot}}^{\text{id}}} \quad (30)$$

are equal when the volumes are the same. If one relaxes this assumption, one would need to solve Eq. (27) with a volume-dependent on i , but we leave this for future work.

Now, we are able to finally write the shear viscosity at finite $\tilde{\mu}$ using an excluded-volume description for a hadron resonance gas

$$\eta^{\text{HRG}} = \frac{5}{64\sqrt{8}} \frac{1}{r^2} \frac{1}{n_{\text{tot}}^{\text{id}}} \sum_i n_i^{\text{id}} \frac{\int_0^\infty k^3 \exp\left(\frac{-\sqrt{k^2+m_i^2}}{T}\right) dk}{\int_0^\infty k^2 \exp\left(\frac{-\sqrt{k^2+m_i^2}}{T}\right) dk}, \quad (31)$$

where the prefactors were derived in [34, 63]. The normalization of η^{HRG} at finite chemical potentials, usually performed with the entropy density at vanishing chemical potentials, requires an excluded-volume calculation for the pressure p^{ex} , as shown already in Eq. (21), and the energy density ε^{ex} ,

$$\varepsilon^{\text{ex}}(T, \mu) = \frac{\varepsilon^{\text{id}}(T, \mu)}{\exp[vp^{\text{ex}}(T, \mu)/T] + vn_{\text{tot}}^{\text{id}}(T, \mu)}, \quad (32)$$

where μ can include all three chemical potentials; see [64] for more details.

Finally, using Eqs. (21) and (32) we compute

$$\frac{\eta^{\text{HRG}} T}{\varepsilon^{\text{ex}} + p^{\text{ex}}} = \frac{\eta^{\text{HRG}} T}{w^{\text{ex}}}, \quad (33)$$

or, in the limit of $\mu \rightarrow 0$ one can simply calculate $\eta^{\text{HRG}}/s^{\text{ex}}$ where the entropy density is $s^{\text{ex}} = \partial p^{\text{ex}}/\partial T|_\mu$. From this point onwards, we will simply discuss η/s or $\eta T/w$ (at finite $\tilde{\mu}$) and drop the index indicating that it has been derived using the excluded-volume formalism.

The radius for the excluded-volume has been tuned to reproduce the lattice QCD entropy (see [36] for the procedure using the PDG2016+ particle list). Here we use the PDG2021+ particle list that does include somewhat more particles. However, these are predominately heavier particles such that their influence does not play a strong role in the calculation of the entropy (rather their influence shows up more in the partial pressures [38]). Thus, the

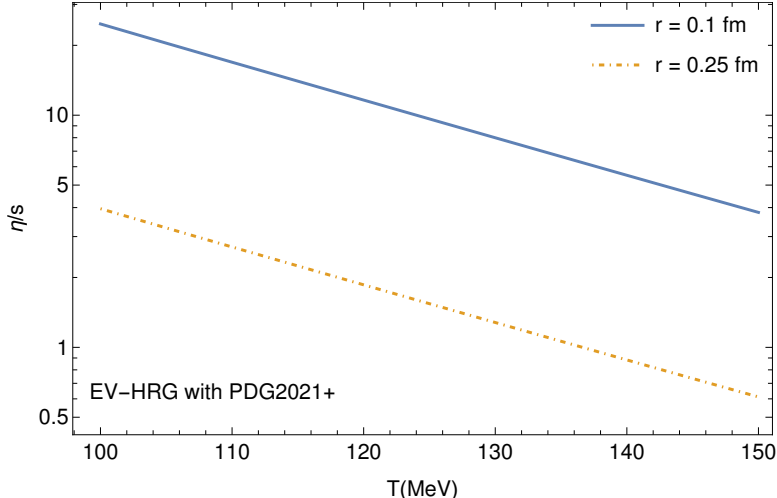


FIG. 5. (color online) η/s from the EV-HRG as a function of the temperature before any rescaling is used. The excluded-volume result for the PDG2021+ list for $r = 0.1$ fm (solid blue) is compared to $r = 0.25$ fm (dash-dotted yellow), both calculated for $\tilde{\mu} = 0$.

previously used range in radii from $r = 0.1$ to 0.25 fm in [36] ends up working well in our study here.

Figure 5 shows a comparison of η/s calculated directly from the HRG between the two choices of radius size, $r = 0.1$ fm and $r = 0.25$ fm in the temperature range relevant for the HRG. The plot makes it clear that shear viscosity is highly dependent on the choice of r wherein the larger r leads to a smaller η/s . If we compare Fig. 5 to Fig. 3 in Ref. [36], we can indeed see that the PDG2021+ lowers η/s . For instance, for the 2016+ list in [36], $\eta/s \sim 1$ at $T = 160$ MeV whereas we find $\eta/s \sim 0.4$ at $T = 160$ MeV for $r = 0.25$ fm. Thus, the addition of new hadronic states lowers η/s in our framework, consistent with previous results [15]. We also note that $r = 0.1$ fm produces an η/s that is extremely large compared to what is anticipated from phenomenology. However, $r = 0.25$ fm is significantly closer to what we would anticipate from extractions of η/s from experimental data.

D. Switching between models

The region close to the first-order transition line cannot be described by either perturbative QCD or an HRG model; thus, we prefer to use an interpolation function to connect the two models. However, there is some freedom on where this interpolation should be applied.

To deal with that, we first consider the chiral phase transition line with just finite μ_B as it is usually defined using a Taylor expansion over the switching temperature:

$$\frac{T_{sw}(\mu_B)}{T_{sw,0}} = \left[1 - \kappa_2 \left(\frac{\mu_B}{T_{sw,0}} \right)^2 - \kappa_4 \left(\frac{\mu_B}{T_{sw,0}} \right)^4 \right], \quad (34)$$

where T_{sw} is the chiral transition temperature, which varies with μ_B , $T_{sw,0}$ is the chiral transition temperature at $\mu_B = 0$, and κ_2 and κ_4 are dimensional parameters that determine the curvature of the transition line in the (μ_B, T_{sw}) plane and whose central values are $\kappa_2 \sim 0.015\text{--}0.016$, $\kappa_4 \sim 0.0003\text{--}0.001$ as taken from lattice QCD from the Wuppertal-Budapest Collaboration [65–67] and the HotQCD collaboration [68]. The transition line drawn by Eq. (34) marks the hypothetical limit between the confined and deconfined phases.

In principle, the extension of Eq. (34) to the case of three conserved charges is easily obtained, i.e.,

$$\frac{T_{sw}(\mu_B, \mu_S, \mu_Q)}{T_{sw,0}} = \left\{ 1 - \sum_{i,j,k} \sum_{X,Y,Z=B,S,Q} \left[\kappa_{i+j=2}^{XY} \left(\frac{\mu_X^i \mu_Y^j}{T_{sw,0}^2} \right) + \kappa_{i+j+k=4}^{XYZ} \left(\frac{\mu_X^i \mu_Y^j \mu_Z^k}{T_{sw,0}^2} \right) \right] \right\}, \quad (35)$$

where mixed terms for BSQ may appear. However, current lattice QCD results [68] only include the diagonal terms for BSQ. Thus, Eq. (35) then simplifies to

$$\frac{T_{sw}(\mu_B, \mu_S, \mu_Q)}{T_{sw,0}} = \left\{ 1 - \sum_{X=B,S,Q} \left[\kappa_2^X \left(\frac{\mu_X}{T_{sw,0}} \right)^2 + \kappa_4^X \left(\frac{\mu_X}{T_{sw,0}} \right)^4 \right] + 2\kappa_{BS} \frac{\mu_B \mu_S}{T^2} \right\}, \quad (36)$$

which is the formula that we will use in this work to describe the behavior of the switching temperatures across the phase diagram. In Table I we list the κ_n^X coefficients that we use in this work, ignoring all the off-diagonal terms. The actual lattice QCD calculations have statistical error bars on their calculations but here we just use the central values (sometimes averaged over collaborations, when possible).

Figure 6 shows the chiral transition line as defined in Eq. (36) and the values in Table I. In this work, we use the form of Eq. (36) to mark the boundary between the HRG and the interpolation function that is defined as $T_{sw,0}^{\text{HRG}} = 156$ MeV and to mark the boundary between the interpolation function and pQCD that is defined as $T_{sw,0}^{\text{pQCD}} = 300$ MeV. We note that the values of $T_{sw,0}^{\text{HRG}}$ and $T_{sw,0}^{\text{pQCD}}$ can easily be varied but at this point we are just attempting to put in reasonable guesses for the range of applicability of these models. However, because the phase transition at vanishing densities is a cross-over, that implies that

n	κ_n^B	κ_n^S	κ_n^Q	κ_n^{BS}
2	0.015	0.017	0.029	-0.0050
4	0.0007	0.004	0.008	n/a

TABLE I. Values used for the κ_n^X coefficients and single available off-diagonal term κ_2^{BS} that describe the slope of the pseudo-critical temperature for the diagonal terms in Eq. (36). These values are averaged central values from different lattice QCD collaborations [65–69]

the transition from hadrons into quarks and gluons does not occur at one fixed temperature but rather a range of temperatures. We point out this fact because different transport coefficients can have inflection points across a range of temperatures as well; see [52, 70] for specific examples.

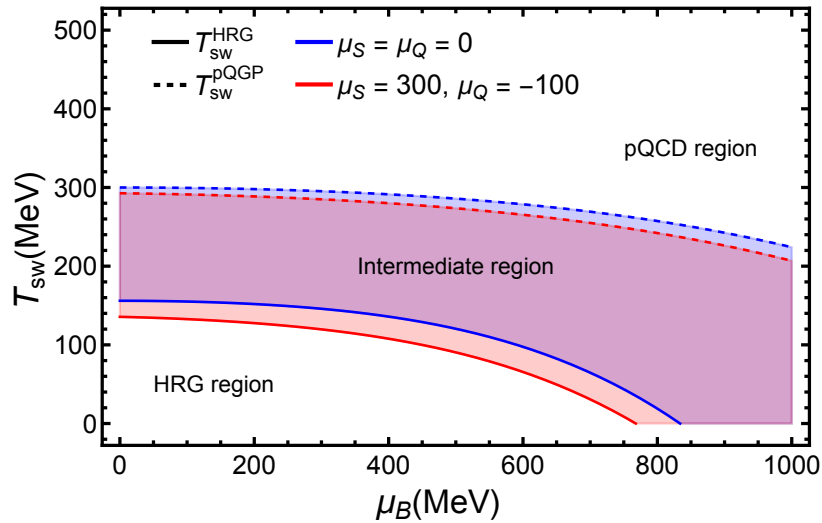


FIG. 6. (color online) Intermediate region between HRG and pQGP regimes, where the switching temperatures are defined by Eq. (36) and the parameter values in Table I, obtained from lattice QCD. In blue, the case of $\mu_S = \mu_Q = 0$ and in red, the case of non-vanishing μ_S and μ_Q . The transition line between the HRG model and the intermediate region is depicted by a solid line and as a dashed line for the transition between intermediate region and the pQCD regime.

III. BUILDING A PHENOMENOLOGICAL MODEL OF THREE CONSERVED CHARGES

In this section, we build the phenomenological model for shear viscosity up to the three conserved charges. We begin by connecting the three different methods we have (HRG, interpolation, pQCD), for the different temperature regimes studied here, separated as follows. Temperatures below the switching line ($T_{\text{sw}} = 156$ MeV for $\mu_B = 0$ MeV), i.e., $T < T_{\text{sw}}$, are studied using the hadron resonance gas model with excluded-volume (EV-HRG). For the region above the switching line, i.e., $T > T_{\text{sw}}$, one expects that pQCD would be the most appropriate description, however, it has been shown by [71–73] that pQCD calculations of thermodynamic observables match lattice calculations at temperatures above $T \gtrsim 300$ MeV for $\mu_B = \mu_S = \mu_Q = 0$ MeV, so our lower boundary was set according to these results. The intermediate region between $T = 156$ MeV to $T = 300$ MeV was calculated using an interpolating function.

As discussed in Sec. II B, shear viscosity for $T > 300$ MeV was obtained using kinetic theory as a function of the BSQ chemical potentials and the strong coupling $1/g^4 \log(g^{-1})$. As a consequence of the logarithmic dependence of the coupling, it is not possible to reach reasonable values without performing a rescaling of these results first. For that purpose, we used the results for η/s obtained by Ghiglieri, Moore, and Teaney (GMT) [13] as follows. We begin by extracting the values of η/s for NLO for a fixed coupling using the two-loop EQCD (Electrostatic QCD [74–78]) value with $\mu_{\text{EQCD}} = (2.7 \leftrightarrow 4\pi)T$. We use these values to match our results at $\mu_B = \mu_S = \mu_Q = 0$ MeV and set the scale for each temperature. Once the rescaling is done for the pQCD results at vanishing densities, the interpolation function can be calculated by simply performing a matching between pQCD and HRG results.

There are infinitely many ways that one could match the HRG to the rescaled pQCD shear viscosity. We generally believe a minimum exists around the cross-over phase transition but have no guidance within full QCD with 2+1 quarks on the nature of that transition. Thus, we choose to use a simple polynomial fit in this work, as defined by

$$F(x) = a + bx + cx^2 + dx^{-1} + fx^{-2}, \quad (37)$$

where a , b , c , d , and f are free parameters that are chosen to ensure that the shear viscosity matches to the HRG and pQCD at their respective transition points. Then, by setting

different coefficients to zero, we obtain different types of fits. For instance, if $c = d = f = 0$ we have a linear fit, and using $d = f = 0$ leads to a quadratic fit.

We ensure that the transition points must always match such that $\eta T/w$ is continuous. As an example, let us explain the matching for a simple linear fitting:

$$F(x) = a + bx, \quad (38)$$

where we have set $c = d = f = 0$ from Eq. (37). At fixed $\tilde{\mu}$, one takes the transition point from the HRG calculation to the interpolation function at $T_{\text{sw}}^{\text{HRG}}(\mu_B)$ where the corresponding shear viscosity is

$$\left(\frac{\eta T}{w}\right)_1 \equiv \frac{\eta T}{w} (T_{\text{sw}}^{\text{HRG}}(\mu_B), \tilde{\mu}), \quad (39)$$

and we also define the transition point from the interpolation function to the pQCD shear viscosity at $T_{\text{sw}}^{\text{pQCD}}(\mu_B)$ where the corresponding shear viscosity is

$$\left(\frac{\eta T}{w}\right)_2 \equiv \frac{\eta T}{w} (T_{\text{sw}}^{\text{pQCD}}(\mu_B), \tilde{\mu}). \quad (40)$$

From Eqs. (39) and (40) we can determine a and b by enforcing continuity. Since this is a linear function, we know that b is the slope such that we can substitute in our two points at $T_1 = T_{\text{sw}}^{\text{HRG}}(\mu_B)$ and $T_2 = T_{\text{sw}}^{\text{pQCD}}(\mu_B)$ to calculate b ,

$$b = \frac{(\eta T/w)_2 - (\eta T/w)_1}{T_{\text{sw},\text{pQCD}} - T_{\text{sw},\text{HRG}}}. \quad (41)$$

We can then substitute in b at either point back into Eq. (38) to obtain a ,

$$a = \left(\frac{\eta T}{w}\right)_1 - \frac{(\eta T/w)_2 - (\eta T/w)_1}{T_{\text{sw}}^{\text{pQCD}} - T_{\text{sw}}^{\text{HRG}}} T_{\text{sw}}^{\text{HRG}}. \quad (42)$$

The same procedure applies for all polynomials of the form of Eq. (37). We can always determine at least two unknowns by this matching procedure where if there are $N > 3$ coefficients, then $N - 2$ coefficients remain as free parameters.

Putting all these pieces together, we can now show different examples of interpolation functions between the two models. In Fig. 7 we compare 4 different choices of interpolating functions where all have minima in $\eta/s(T)$ at $\tilde{\mu} = 0$. Note that the pQCD results in Fig. 7 are already rescaled according to the GMT results from [13], and we use an excluded-volume HRG with $r = 0.25$ fm. Comparing the HRG to pQCD at their transition points at $\vec{\mu} = \{\mu_B, \mu_S, \mu_Q\} = 0$, we see that the HRG is somewhat higher but that they are reasonably close to each other such that matching between the two is acceptable.

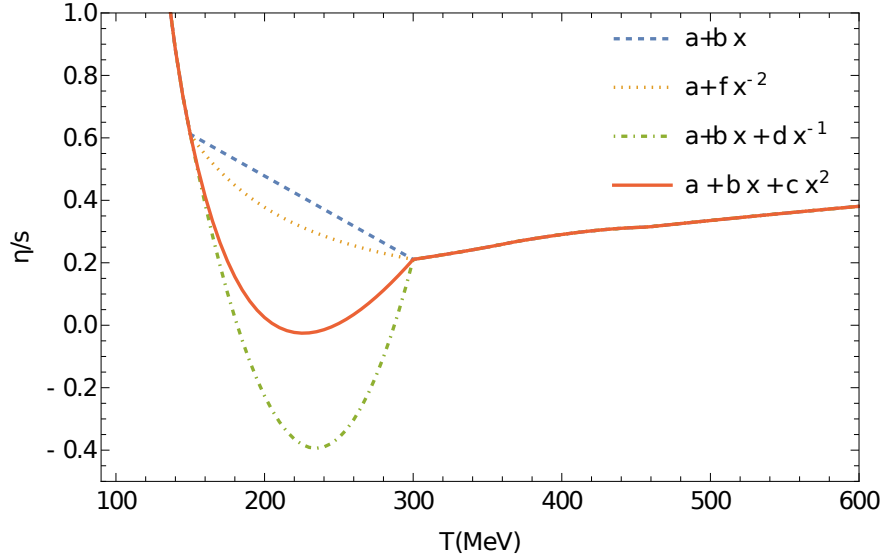


FIG. 7. (color online) Different functional forms connecting the HRG shear viscosity at low T and $r = 0.25$ fm to rescaled pQCD shear viscosity to match the results from Ref. [13] at high T .

One can see in Fig. 7 that the location and overall value of the minimum $(\eta/s)_{min}$ depends strongly on the functional form of our interpolation function. In fact, some functional forms lead to nonphysical values of $\eta/s < 0$. For the following work, when we obtain values of $\eta T/w < 0$ then we simply reset $\eta T/w \equiv 0$. Thus, we ensure the positivity of shear viscosity, which is consistent with stability constraints for relativistic viscous fluids [79, 80] and statistical mechanics [81, 82]. However, we generally suggest that one should choose a functional form at least at $\vec{\mu} = 0$ that avoids $\eta/s < 0$.

Out of the different functional forms that we used in Fig. 7, the form $a + bx + dx^{-1}$ (red curve in Fig. 7) looks the most like what one would expect from a Bayesian analysis, in that it has a minimum in η/s around the cross-over phase transition. It also avoids any issues with negative values of η/s . That being said, that form has an extra free parameter that we must select by hand. Thus, we choose to take the next by option of $a + bx$ (blue curve in Fig. 7) that only has two coefficients such that they are both fixed by the transition points. Our a and f coefficients are determined independently along slices of $\vec{\mu}$.

As a final comment to Fig. 7, the overall magnitude (especially at high and low T) is likely significantly too high compared to what one anticipates from the extraction of $\eta/s(T)$ using Bayesian analyses [6–9]. Thus, in the following, we also implement an overall normalization constant g_{norm} such that we can shift the functional form up- or downward. One may

wonder why we use microscopic approaches and then implement an overall normalization factor. The reason is that we are primarily interested in obtaining models with a finite $\tilde{\mu}$ behavior such that given an η/s at $\tilde{\mu} = 0$ we can then use this approach to extrapolate to finite $\tilde{\mu}$. Thus, because both the HRG and pQCD shear viscosities have rather non-trivial behaviors, especially considering all three conserved charges, we can explore some interesting behaviors at finite $\tilde{\mu}$.

Free Parameters	
Parameter	Default Value
$(\eta/s)_{\text{set}}$	0.08
$T_{\text{sw}}^{\text{HRG}}$	156 MeV
$T_{\text{sw}}^{\text{pQCD}}$	300 MeV
r	0.25 fm
Constrained Parameters	
Parameter	Source
g_{norm}	$(\eta/s)_{\text{set}}/(\eta/s)_{\text{min}}$
g_{GMT}	$(\eta/s)_T^{\text{pQCD}}/(\eta/s)_T^{\text{GMT}}$ [13]
a, b, c, d, f	determined from matching

TABLE II. Free and constrained parameters in our phenomenological construction of $\eta T/w$.

In summary, our shear viscosity algorithm is

$$\left(\frac{\eta T}{w}\right)_{\text{tot}}(T, \tilde{\mu}) = g_{\text{norm}} \begin{cases} \left(\frac{\eta T}{w}\right)_{\text{HRG}} & T < T_{\text{sw}}^{\text{HRG}} \\ \left(\frac{\eta T}{w}\right)_{\text{intermediate}} & T_{\text{sw}}^{\text{HRG}} < T < T_{\text{sw}}^{\text{pQCD}} \\ g_{\text{GMT}} \left(\frac{\eta T}{w}\right)_{\text{pQCD}} & T > T_{\text{sw}}^{\text{pQCD}} \end{cases} \quad (43)$$

where g_{GMT} is the scaling factor to reproduce the pQCD results from [13] at $\tilde{\mu} = 0$ and g_{norm} is the overall normalization constant that can be constrained at $\tilde{\mu} = 0$.

In Table II, we summarize all the parameters used in our approach. We have two types of parameters, free parameters and constrained parameters. For the constrained parameters g_{norm} is constrained by $(\eta/s)_{\text{set}}$ and the details of the rest of the calculation that lead to a certain minimum of η/s at $\mu_B = 0$ MeV; g_{GMT} is determined from the calculations in Ref. [13]. Lastly, at least two of the coefficients a, b, c, d , and f are determined from our matching

procedure. The remaining free parameters are not entirely free. The value of $(\eta/s)_{\text{set}}$ is guided by experimental data, $T_{\text{sw}}^{\text{HRG}}$ and $T_{\text{sw}}^{\text{pQCD}}$ should be reasonable values that are guided by comparisons of the HRG and pQCD results to lattice QCD, and r is constrained within the given range if one uses PDG2021+ in order to reproduce lattice QCD thermodynamic results.

IV. RESULTS FOR $\eta T/w$

Below we discuss the results for our phenomenological $\eta T/w$. We begin with the results for just one conserved charge, i.e., baryon density and then we consider the implications of all three conserved charges. For our results, we cannot show the strangeness neutral case because the interpolation function does not provide information about the densities (since the matching is done at fixed $\tilde{\mu}$) such that the conditions in Eq. (17) cannot be fulfilled. Rather, if one were to use our $\eta T/w$ within a relativistic fluid dynamic code, then one would be able to determine the strangeness neutral trajectory via a chosen equation of state. In other words, the strangeness neutral trajectory in our approach is equation of state dependent.

A. $\eta T/w$ at finite μ_B and overall magnitude

In Fig. 8, we show the result of our $\eta T/w$ for $\mu_B = 0-600$ MeV where in this case, we have not yet included an overall rescaling, i.e., $g_{\text{norm}} = 1$. The left panel in Fig. 8 shows the calculation using $r = 0.1$ fm in the HRG phase, and the right plot shows the $r = 0.25$ fm case in the HRG phase. In both cases, the pQCD sector has the same renormalization to GMT at $\tilde{\mu} = 0$ (as described previously). The region calculated with our interpolation function in Eq. (37) is marked with big dots on both edges. We find a rather non-trivial difference between $r = 0.1$ fm and $r = 0.25$ fm in that $r = 0.25$ fm leads to a $(\eta T/w)_{\text{min}}$ at lower temperatures at large μ_B because its magnitude in the HRG phase is lower. That implies that the minimum of $\eta T/w$ shifts to lower values of T as μ_B increases, which is what we would expect.

Another finding is that the $r = 0.1$ fm has all the $(\eta T/w)_{\text{min}} \sim 300$ MeV, which occurs because $\eta T/w$ in the HRG phase is extremely high to the point that it is most likely incom-

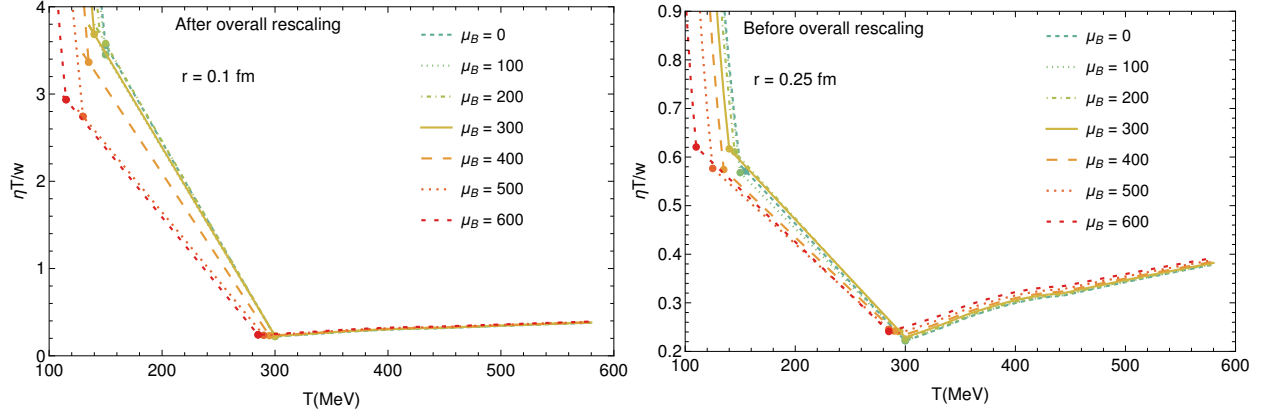


FIG. 8. (color online) Left: $\eta T/w$ as a function of the temperature for each value of μ_B in MeV for $r = 0.1$ fm. Right: $\eta T/w$ as a function of the temperature for each value of μ_B for $r = 0.25$ fm. The results are shown before an overall rescaling is applied (i.e., $g_{\text{norm}} = 1$), but do include the pQCD rescaling.

patible with collective flow results calculated using relativistic hydrodynamics. Additionally, in the case of $r = 0.1$ fm there is a significant mismatch in the overall magnitude of $\eta T/w$ in the HRG and pQCD limits such that the pQCD effectively has no finite $\vec{\mu}$ dependence. However, one issue is that the $\eta T/w$ in Fig. 8 are still above the KSS bound [5] and differ in magnitude from what is seen in the Bayesian analyses. Thus, we will use our scaling factor g_{norm} to readjust the magnitude of η/s at $\vec{\mu} = 0$ to obtain values that are more reasonable compared to experimental data. Then, g_{norm} remains constant across $\vec{\mu}$. For that, we follow the same procedure as in [36] to scale shear viscosity to match what is expected from experimental data:

- Find the minimum value of $(\eta/s)_{\text{min}}$ at $\mu_B = 0$ MeV. With that, we identify T_{min} as being the temperature where $(\eta/s)_{\text{min}}$ has its minimum value for $\mu_B = 0$ MeV.
- Then we can determine g_{norm} from

$$g_{\text{norm}} = \frac{(\eta/s)_{\text{set}}}{(\eta/s)_{\text{min}}}, \quad (44)$$

where we have chosen $(\eta/s)_{\text{set}} \equiv 0.08$ to be the new minimum of η/s at $\mu_B = 0$ MeV in the following results.

Since $(\eta/s)_{\text{set}}$ is a free parameter in our code, one could choose other values, if needed. In principle, one could use a data-driven approach to determine $(\eta/s)_{\text{set}}$ as well as the other

free parameters discussed in Table II. However, we leave such a study for future work. We note here that the point of this work is not to obtain the perfect behavior of $\eta/s(T)$ at vanishing densities (because of all the caveats with the overall magnitudes of η/s coming directly from our models) but rather to use these models to obtain a reasonable behavior across μ_B , μ_S , and μ_Q since there is very little guidance from both theory and experiments on $\eta T/w$ at finite densities.

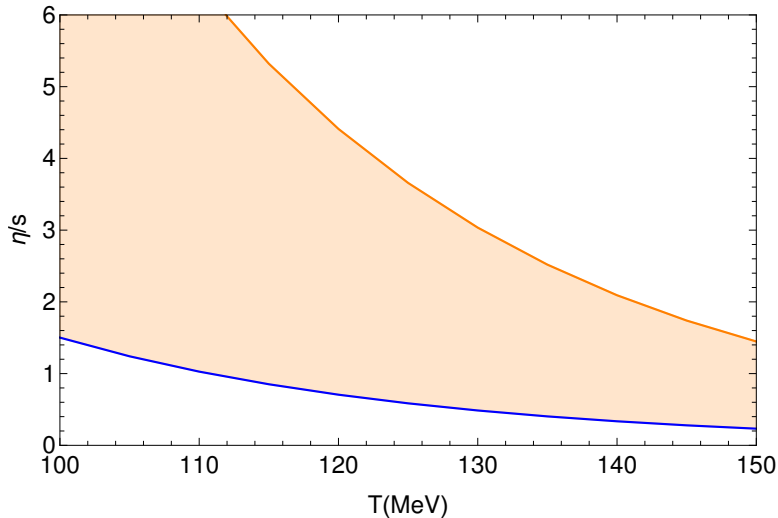


FIG. 9. (color online) η/s as a function of the temperature for (orange) $r = 0.1$ fm and (blue) for $r = 0.25$ fm. The shaded region corresponds to the uncertainty in our calculations due to the effective core radius choice.

From here on, we will now set $(\eta/s)_{\text{set}} = 0.08$ such that $g_{\text{norm}} \neq 1$. The value of g_{norm} only shifts the overall magnitude of $\eta T/w$ but does not change the behavior across the T and μ_B such that this behavior comes from the models themselves. Figure 9 shows the renormalized η/s at $\tilde{\mu} = 0$ for the two different values of $r = 0.1$ fm (orange) and $r = 0.25$ fm (blue). One can easily see that even after the overall rescaling, the values of η/s in the hadronic phase for $r = 0.1$ fm are still very large compared to what is expected from other hadronic approaches like SMASH [37]. Thus, for the remainder of this work we focus only on the $r = 0.25$ fm case because it leads to results that are more reasonable in magnitude and has a relevant finite $\tilde{\mu}$ dependence for the pQCD limit.

We now study our shear viscosity at finite μ_B , using our formalism. As explained before, we use the same functional form at finite μ_B but the coefficients in the function form depend

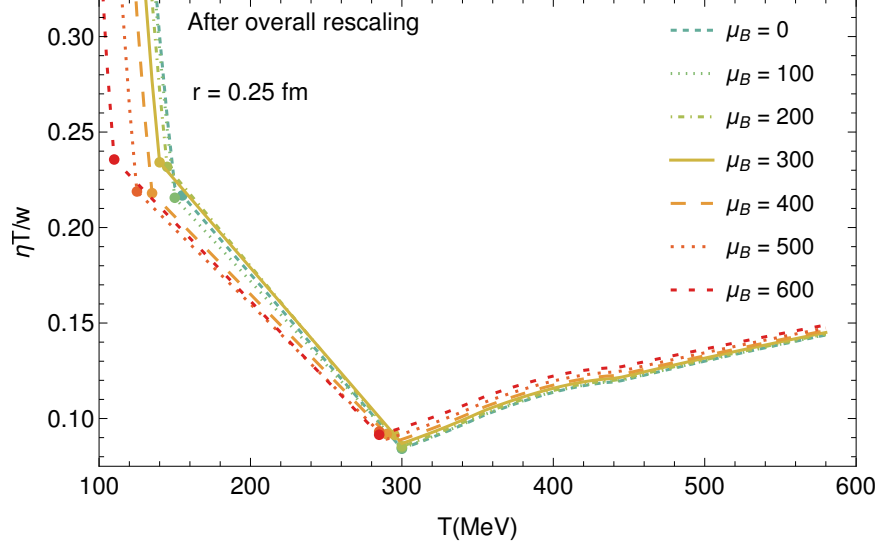


FIG. 10. (color online) $\eta T/w(T, \mu_B)$ along different slices of μ_B in MeV for $r = 0.25$ fm. Here, we show the curves with the overall rescaling g_{norm} . The large dots show the interpolation region on the plot.

on μ_B since they are determined at the matching points at both high and low temperatures to the pQCD and HRG results. In Fig. 10 we plot our results at finite μ_B for $r = 0.25$ fm where we have included the rescaling. We find that our approach leads to a very non-trivial behavior. Because the shear viscosity in the HRG phase at the transition point is generally higher than the shear viscosity at the pQCD transition point, i.e.,

$$\frac{\eta T}{w}(T_{\text{sw}}^{\text{HRG}}(\mu_B), \mu_B) > \frac{\eta T}{w}(T_{\text{sw}}^{\text{pQCD}}(\mu_B), \mu_B), \quad (45)$$

then, the minimum in $\eta T/w$ for a fixed μ_B ends up being at $T \sim 300$ MeV. Of course, if one used a different type of interpolation function, one could adjust the location of the minimum, this just happens to be a consequence of the specific choice made here. One other effect that we see is that due to the drop in T_{sw} at finite μ_B , the $\eta T/w(T_{\text{sw}}^{\text{HRG}}(\mu_B), \mu_B)$ ends up increasing quite a bit at large μ_B . In contrast, the transition point between pQCD and the interpolation does not vary nearly as strong with μ_B and therefore remains close to $\eta T/w(T_{\text{sw}}^{\text{pQCD}}(\mu_B), \mu_B) \sim (\eta/s)_{\text{set}}$.

In Figs. 8–10 we can also study the dependence of the HRG phase on T and μ_B . Generally, the HRG has a significantly steeper slope in T than the pQCD phase. Additionally, we find in our setup that the HRG also has a stronger μ_B dependence than the pQCD phase. For a fixed T but increasing μ_B we find that $\eta T/w$ for the HRG regime consistently decreases

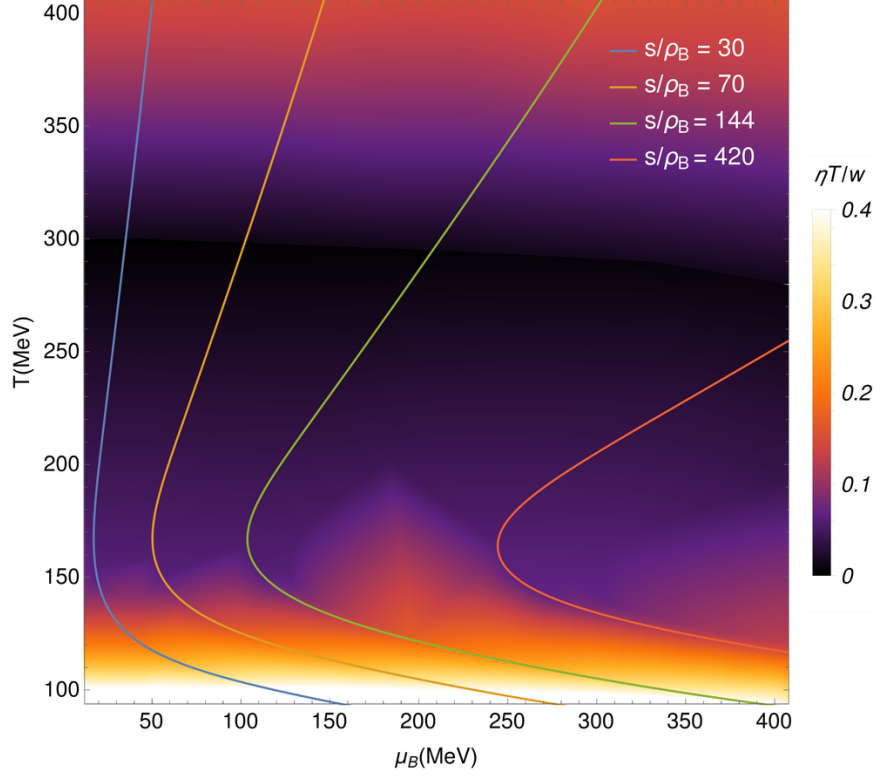


FIG. 11. (color online) $\eta T/w$ considering an effective radius $r = 0.25$ fm for isentropes trajectories along the QCD phase diagram. The colors indicate the different isentropes defined by s/ρ_B .

and for a fixed μ_B but increasing T the $\eta T/w$ for the HRG regime consistently decreases as well. Thus, the HRG regime has the complete opposite behavior compared to the pQCD phase, wherein the pQCD regime increases with increasing T and also μ_B . The difference in how $\eta T/w$ behaves in the HRG vs pQCD regime can be understood as follows: in the hadronic phase, we use a geometric cross-section to account for all the scatterings in the system, as the number of particles increases and the scatterings become more frequent, this system tends to equilibrate faster.

To summarize our finite μ_B study, we plot a density plot of $\eta T/w$ across the (T, μ_B) phase diagram. As expected from our other plots, around the phase transition a minimum in $\eta T/w$ is seen from $T \sim 156$ – 300 MeV. At low temperatures, we see a sharp increase in $\eta T/w$ due to the HRG phase. In the range of $\mu_B = 0$ – 400 MeV there is almost no μ_B dependence but beyond that point ($\mu_B \gtrsim 400$ MeV) we begin to see a stronger μ_B dependence.

If the system were explored by an ideal fluid, then both entropy and baryon number would be conserved such that isentropes of entropy density s over baryon density ρ_B would

be exactly conserved. Comparing to isentropes can then provide some idea of how an actual heavy-ion collision would “see” the viscosity as it expands and cools through the QCD phase diagram. The heavy-ion collisions would start at the high T , high μ_B end of the isentrope and as it cools it drops in both T and μ_B until it hits the phase transition where the isentropes bend back and μ_B begins to increase again. At some point, shortly after the phase transition, the particles are expected to freeze-out such that the isentrope trajectory is no longer followed down to low T and large μ_B . As a quick note, $s/\rho_B \neq \text{const.}$ in an actual heavy-ion collision because of entropy production, which is especially relevant around a critical point [83–85]. However, even the out-of-equilibrium trajectories are related to the isentropes [84] such that they can still provide some guidance for what one can expect in experiments.

In Fig. 11, we also plot the isentropes, s/ρ_B , for trajectories relevant to the Beam Energy Scan at RHIC. The isentropes are shown in colored lines laid on top of the density plot of $\eta T/w$. Because this range of μ_B does not yet have a strong μ_B dependence, then the path from the isentrope is not that different from what is already shown along slices of fixed μ_B . Probably the biggest effect from the path of an isentrope vs a slice across T at fixed μ_B is that for small values of s/ρ_B (corresponding to lower beam energies \sqrt{s}) is that the isentrope bends towards large μ_B as T increases. The effect is that the isentropic trajectory remains in the low $\eta T/w$ regime for a longer period of time (in contrast to something that would just increase in T).

V. $\eta T/w$ IN THE PRESENCE OF THREE CONSERVED CHARGES

In this section, we show our final results for shear viscosity along the QCD phase diagram for multiple conserved charges. As there is no good way of displaying a 4D representation of $\eta T/w$, we will build up from one conserved charge up to three. We already showed the case where $\mu_B > 0$ and $\mu_S = \mu_Q = 0$ MeV, shown in Figs. 10 and 11 in the previous section. We begin in Fig. 12 by comparing the limits of $\mu_B > 0$ with $\mu_S = \mu_Q = 0$ MeV, $\mu_S > 0$ with $\mu_B = \mu_Q = 0$ MeV, and $\mu_Q > 0$ with $\mu_B = \mu_S = 0$ MeV. Figure 12 is similar to what was previously shown for pQCD in Fig. 2 but here we have matched to the HRG. For the range of chemical potentials considered here, the pQCD results for $\eta T/w$ are nearly the same for μ_B is finite and for μ_S is finite. However, the HRG results find that a finite μ_S

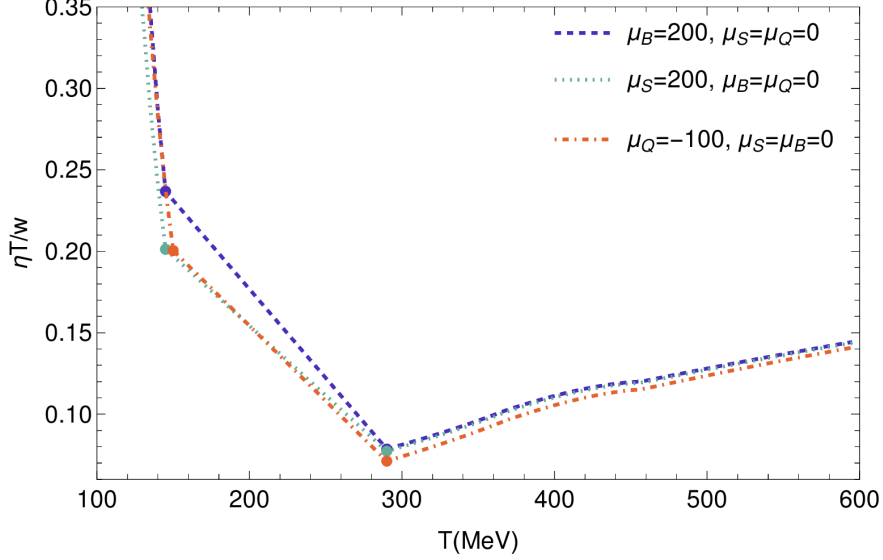


FIG. 12. (color online) $\eta T/w$ as a function of the temperature for $r = 0.25$ fm comparing the three scenarios of $\mu_B > 0$ with $\mu_S = \mu_Q = 0$ MeV, $\mu_S > 0$ with $\mu_B = \mu_Q = 0$ MeV, and $\mu_Q > 0$ with $\mu_B = \mu_S = 0$ MeV. The large dots show the interpolation region on the plot.

leads to a suppression of $\eta T/w$ in the HRG phase. Thus, at temperatures $T < 300$ MeV, the differences between the chemical potentials become more clear, and there is a hierarchy wherein a finite μ_B has the largest $\eta T/w$, then finite μ_Q , and a finite μ_S leads to the smallest $\eta T/w$. This hierarchy differs from what was seen for pQCD (μ_S and μ_Q switch).

We note that we are limited to a smaller range in μ_Q within our approach than for μ_B and μ_S . The reason for this limitation is that a singularity appears in the Bose-Einstein distribution at the point where $m_\pi = \mu_Q$. To understand this better, we can look at the Bose-Einstein distribution when the momentum goes to zero for the pions,

$$\begin{aligned}
 f_\pi(k=0) &= \sum_{Q=\pm 1} \frac{1}{e^{E_\pi(k)/T - Q\mu_Q/T} - 1} \\
 &= \frac{1}{e^{(m_\pi - \mu_Q)/T} - 1} + \frac{1}{e^{(m_\pi + \mu_Q)/T} - 1},
 \end{aligned} \tag{46}$$

where we have substituted in $E_\pi = \sqrt{m_\pi^2 + k^2}$ in the limit of the momentum going to zero $k \rightarrow 0$ such that $E_\pi = m_\pi$. Then, at the point that $m_\pi = \pm\mu_Q$ we obtain a singularity. To avoid this problem, we always keep $|\mu_Q| < m_\pi$ in this work. Analogously, one could find a similar point for kaons, i.e.,

$$f_K(k=0) = \frac{1}{e^{(m_K - \mu_Q - \mu_S)/T} - 1} + \frac{1}{e^{(m_K + \mu_Q + \mu_S)/T} - 1}, \tag{47}$$

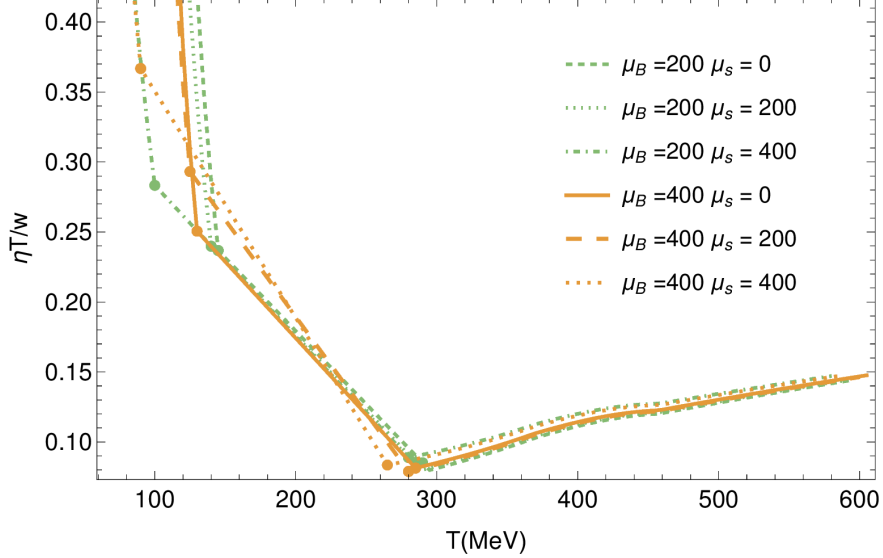


FIG. 13. (color online) $\eta T/w$ as a function of the temperature for each value of μ_B and μ_S for $r = 0.25$ fm. The transition points to the interpolation region are indicated with closed-circle markers.

where we have a singularity at $m_K = \pm(\mu_Q + \mu_S)$. Therefore, we always ensure that $|\mu_Q + \mu_S| < 500$ MeV to avoid any issues with the singularity. Finally, we point out that baryons do not run into this same issue because the Fermi-Dirac distribution has a (+1) factor in the denominator instead of a (-1) from the Bose-Einstein distribution such that no singularity appears.

Next, we study a mixture of finite μ_B and μ_S in Fig. 13. There, the green lines are for $\mu_B = 200$ MeV, and the orange lines are for $\mu_B = 400$ MeV; the variation in μ_S is shown by different line styles. If we first study $\mu_B = 200$ MeV we find that the effect of μ_S is very small in the range of $\mu_S = 0$ –200 MeV both for the pQCD and HRG regimes such that there is almost no discernible change. However, at $\mu_B = 200$ MeV and $\mu_S = 400$ MeV then $\eta T/w$ shifts to higher values in the pQCD regime and lower values in the HRG, effectively flattening out $\eta T/w$ a bit. We also see for that combination of μ_B and μ_S that there is a strong shift in the transition between interpolation and HRG to lower values of T such that the HRG calculation only appears around $T \sim 100$ MeV.

Now, looking at $\mu_B = 400$ MeV we find that μ_S is playing a larger role when it is switched on. The larger μ_B is much more sensitive to the influence of μ_S . The pQCD regime is not so strongly influenced, however, the HRG shifts both to larger $\eta T/w$ when μ_S switched on.

Additionally, at both finite μ_S and μ_B we see a stronger shift in the HRG to lower $T_{\text{sw}}^{\text{HRG}}$ across the transition from interpolation to HRG. We can understand this because in the Fermi-Dirac/Bose-Einstein distributions, the influence of $\vec{\mu}$ is normalized by T (i.e., $\vec{\mu}/T$) such that when there is a shift to lower T we expect a stronger influence from changes in $\vec{\mu}$. We note that the shift in $T_{\text{sw}}^{\text{pQCD}}$ is much smaller for a fixed $\vec{\mu}$ than it is for $T_{\text{sw}}^{\text{HRG}}$ because the Taylor series in Eq. (36) scales with μ/T_0 where the larger value of $T_{\text{sw},0}^{\text{pQCD}}$ implies that a larger μ is needed to see the same effect (compared to $T_{\text{sw}}^{\text{HRG}}$). However, the effect of μ_B in the presence of μ_S does have a stronger influence in the HRG regime.

Finally, we compare the scenario for $\eta T/w$ when all three chemical potentials are finite, i.e., $\mu_Q > 0$, $\mu_B > 0$, and $\mu_S > 0$ in Fig. 14 plotted as a function of temperature T . In principle, we could plot many combinations of μ_B, μ_S, μ_Q but an easy way to demonstrate the effect of μ_Q is to keep μ_B and μ_S fixed and just vary μ_Q . Here we specifically choose both positive and negative values of μ_Q to understand the interplay between chemical potentials. Additionally, we are careful to ensure that the combination of $|\mu_S + \mu_Q| < 500$ MeV to avoid any issue from the singularity coming from kaons. We find in Fig. 14 that $\mu_Q < 0$ has an overall larger $\eta T/w$ than $\mu_Q > 0$ in the HRG phase, and the opposite happens in the pQCD phase (the influence is largest in the HRG phase). Thus, a positive, large μ_Q ends up having a flatter $\eta T/w$ across T compared to a negative μ_Q . Overall, it is clear that when one allows for fluctuations in BSQ conserved charges then it is possible to produce a rather non-trivial dependence on $\vec{\mu}$ for $\eta T/w$.

A. Fixing $\eta T/w$ at the transition points

Up until this point, we have allowed the calculations of $\eta T/w$ from HRG and pQCD to determine the value of $\eta T/w(T_{\text{sw}}^{\text{HRG}}(\mu_B), \mu_B)$ and $\eta T/w(T_{\text{sw}}^{\text{pQCD}}(\mu_B), \mu_B)$ at the transition points. In the case of the pQCD results, the overall magnitude is fairly well motivated from NLO calculations, although convergence has not yet been shown in the series, such that NNLO may change the behavior further. In the case of the HRG results, the magnitude depends on a correlated combination between the number of hadronic states in the system, their masses, and the excluded-volume extracted from comparisons with lattice QCD. Additionally, the HRG calculations depend on the assumption of a fixed volume for all hadrons. If one were to eventually measure further hadronic states or include more complicated inter-

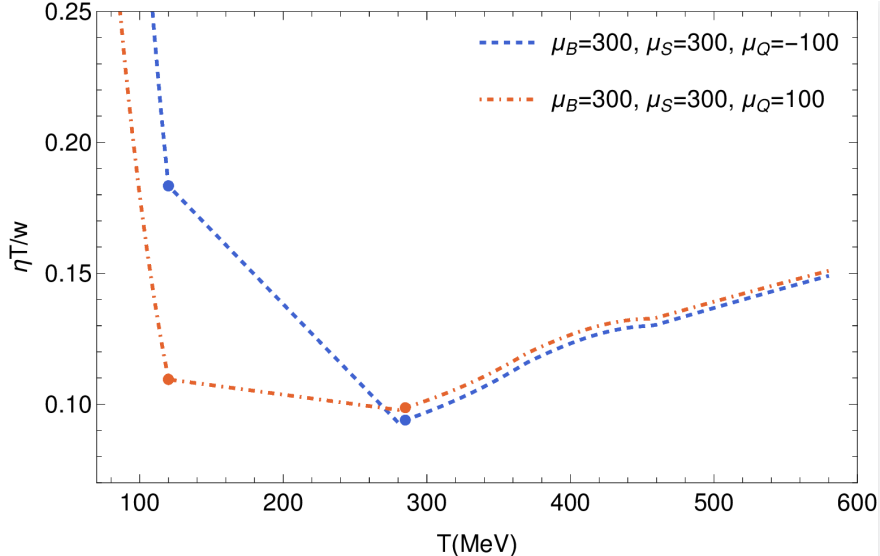


FIG. 14. (color online) $\eta T/w$ as a function of the temperature for $r = 0.25$ fm when all three chemical potentials are finite. Here we hold $\mu_B = \mu_S = 300$ MeV fixed and vary only $\mu_Q = \pm 100$ MeV.

actions, then the overall magnitude may change. Thus, it is an interesting question how the finite $\vec{\mu}$ behavior looks like if we fix $\eta/s(T_{\text{sw}}^{\text{HRG}}(0), 0) = \eta/s(T_{\text{sw}}^{\text{pQCD}}(0), 0)$ at the transition regime at $\vec{\mu} = 0$ and allow the finite $\vec{\mu}$ behavior to come from the HRG and pQCD regimes. In other words, we scale η/s from the HRG and pQCD regimes to have the same minimum at $\vec{\mu} = 0$ such that we can study how their $\vec{\mu}$ behavior compares to each other.

μ_B (MeV)	μ_S (MeV)	μ_Q (MeV)
400	0	0
400	400	0
0	400	0
400	300	-100
400	300	+100

TABLE III. Combination of chemical potentials used in Fig. 15 when rescaling the pQCD and HRG regimes to be of the same overall values at their minima.

In Fig. 15, we show the results of fixed η/s at the transition point at vanishing densities. We choose combinations of chemical potentials to highlight different regimes of the phase diagram, shown in Table III. These values are chosen to ensure that neither the pion or

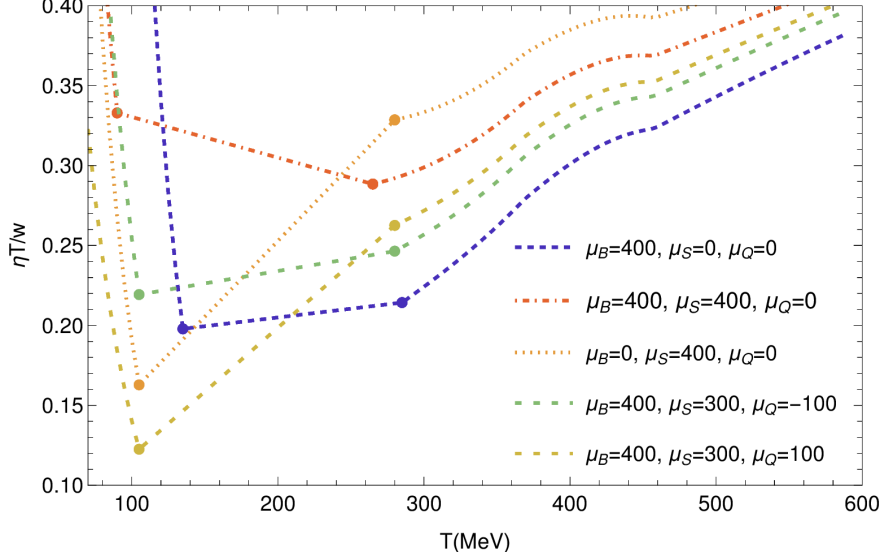


FIG. 15. (color online) We scale η/s for the HRG and pQCD to be identical at the transition points for $\vec{\mu} = 0$, i.e., $\eta/s(T_{\text{sw}}^{\text{HRG}}(0), 0) = \eta/s(T_{\text{sw}}^{\text{pQCD}}(0), 0)$. Then, $\eta T/w$ is shown as a function of the temperature in MeV for $r = 0.25$ fm for a variety of $\vec{\mu}$. The large dots show the interpolation region on the plot.

kaon singularity are reached in the HRG phase. We find that $\eta T/w$ from pQCD grows more slowly with T and has a small bump around $T \sim 400$ MeV for all combinations of chemical potentials. In contrast, the HRG phase sharply drops when T increases and it is always a monotonically decreasing $\eta T/w$.

Regardless of the combination of chemical potentials, one can see in Fig. 15 that the magnitude of the change across $\vec{\mu}$ is relatively similar for both the HRG vs the pQCD regime when we rescale their overall magnitudes at the transition region. For our chosen chemical potentials and T range, pQCD ranges from $\eta T/w \sim [0.2, 0.4]$ whereas the HRG ranges from $\eta T/w \sim [0.1, 0.4]$. This effect (that the magnitude of change across $\vec{\mu}$ is similar for pQCD and HRG) was not evident in the previous plots because of our approach algorithm that is motivated both by the physics of pQCD at vanishing densities and also results from Bayesian analyses that demonstrate a nearly flat η/s at $\vec{\mu} = 0$. Thus, our previous results allowed for the pQCD regime to have a much smaller overall magnitude of $\eta T/w$ such that its scaling across $\vec{\mu}$ was suppressed. At the time of writing this paper, we do not know what the “correct” answer is. Should the HRG and pQCD regimes have similar values of $\eta T/w$? Or does the HRG phase have an overall larger value? The answer to that question will then

dictate how strongly $\eta T/w$ varies with $\vec{\mu}$ in the high T regime (and also will influence the interpolation regime).

We can then compare the interplay between the μ_B, μ_S, μ_Q behavior between the HRG and pQCD regimes. We can use the blue line in Fig. 15 ($\mu_B = 400$ MeV) as a baseline wherein only the baryon chemical potential is switched on. Comparing this to the limit of $\mu_S = 400$ MeV (orange dotted line), we find that the effect of μ_S increases $\eta T/W$ in the pQCD regime and decreases $\eta T/W$ in the HRG such that the overall $\eta T/W$ at finite μ_S has a narrow minimum at $T \sim 100$ MeV and then grows steeply with T . For the case of $\mu_B = \mu_S = 400$ MeV the HRG regime increases $\eta T/w$. Finally, we compare the scenario where all three chemical potentials are finite, i.e., $\mu_B = 400$ MeV, $\mu_S = 300$ MeV, and $\mu_Q = \pm 100$ MeV (note that we lower μ_S to avoid the kaon singularity). When we have finite μ_B, μ_S and vary μ_Q we find that $\mu_Q < 0$ flattens $\eta T/w$ across T because the HRG and pQCD results are similar in value at the transition points. However, finite μ_B, μ_S and $\mu_Q > 0$ we find a much sharper behavior in $\eta T/w$ across T wherein a minimum of $\eta T/w$ occurs at low T .

VI. CONCLUSIONS AND OUTLOOK

We used pQCD results with three conserved charges and a hadron resonance gas picture with a state-of-the-art list of resonances to study the QCD shear viscosity at large baryon densities. We have applied a phenomenological approach to produce curves of $\eta T/w(T, \mu_B, \mu_S, \mu_Q)$ across the QCD phase diagram, which can be used to feed relativistic viscous hydrodynamic codes simulating collisions at energies covered by the RHIC Beam Energy Scan or BSQ fluctuations of conserved charges at the LHC. Here, we considered three scenarios, one conserved charge ($\mu_B \neq 0$ with $\mu_S = \mu_Q = 0$ MeV), two conserved charges ($\mu_B \neq 0$ and $\mu_S \neq 0$ with $\mu_Q = 0$ MeV) and three conserved charges ($\mu_B \neq 0$ and $\mu_S \neq 0$ and $\mu_Q \neq 0$ MeV). With that, we have presented the first study of $\eta T/w$ with three conserved charges along the QCD phase diagram and developed an easily reproducible procedure that could rely on other models to calculate $\eta T/w$ as well (e.g., holography, hadron transport, etc.). We believe that this could also be performed for different transport coefficients, such as bulk viscosity, which might be more sensitive to critical scaling [55, 83, 84, 86–88].

We find a non-trivial relationship between μ_B, μ_S , and μ_Q , especially in the pQCD regime

since $\mu_S > 0$ generally increases $\eta T/w$, $\mu_Q > 0$ decreases $\eta T/w$, and $\mu_B > 0$ has a non-monotonic behavior. The strangeness neutral trajectory generally has $\mu_B > 0$, $\mu_S > 0$, and $\mu_Q < 0$ such that one may expect that $\eta T/w$ decreases with increasing μ_B in the pQCD regime. However, fluctuations in BSQ are anticipated around the strangeness neutral trajectory such that one requires full relativistic viscous hydrodynamic simulations to truly understand the consequences. In the HRG regime, large $\vec{\mu} > 0$ generally decreases $\eta T/w$ if one looks at a fixed T . However, $T_{\text{sw}}^{\text{HRG}}$ decreases as one increases $|\vec{\mu}|$ such that $\eta T/w$ is large (since $\eta T/w$ grows rapidly as T decreases). While $\eta T/w$ generically decreases as one switches on any of the chemical potentials, how much it decreases depends on if one switches μ_B , μ_S , or μ_Q (μ_S shows the strongest suppression). Thus, the combination of all three chemical potentials and the effect of the transition region (also with 3 chemical potentials) leads to non-monotonic changes in $\eta T/w$ across the phase diagram.

There is still space for improvement, as leading-order or even next-leading-order calculations can also be performed for multiple chemical potentials, giving a more detailed description of shear viscosity in the high-temperature regime. Additionally, the HRG regime could be further improved by allowing for different types of interactions (here we always used a constant excluded-volume across all hadrons). However, even with these challenges ahead, our framework opens up the doorway to performing Bayesian analyses with $\eta T/w$ at finite μ_B , μ_S , and μ_Q . One could perform a Bayesian analysis, for instance, varying the overall normalization constant at $\vec{\mu} = 0$, the type of interpolation region, and the transition temperatures at $\vec{\mu} = 0$.

ACKNOWLEDGMENTS

The authors would like to thank Guy D. Moore and Jorge Noronha for instructive conversations. I.D. acknowledges the support by the State of Hesse within the Research Cluster ELEMENTS (Project ID 500/10.006), and support by the Deutsche Forschungsgemeinschaft (DFG, German Research Foundation) through the CRC-TR 211 ‘Strong-interaction matter under extreme conditions’– project number 315477589 – TRR 211. J.S.S.M. is supported by Consejo Nacional de Humanidades, Ciencias y Tecnologías (CONAHCYT) under SNI Fellowship I1200/16/2020. J.N.H. acknowledges support from the US-DOE Nuclear Science Grant No. DE-SC0020633, DE-SC0023861, and within the framework of the Saturated Glue

(SURGE) Topical Theory Collaboration. The work is also supported from the Illinois Campus Cluster, a computing resource that is operated by the Illinois Campus Cluster Program (ICCP) in conjunction with the National Center for Supercomputing Applications (NCSA), and which is supported by funds from the University of Illinois at Urbana Champaign. This work was supported in part by the National Science Foundation (NSF) within the framework of the MUSES collaboration, under grant number OAC-2103680.

- [1] K. Adcox et al. (PHENIX), *Nucl. Phys. A* **757**, 184 (2005), [arXiv:nucl-ex/0410003](#).
- [2] I. Arsene et al. (BRAHMS), *Nucl. Phys. A* **757**, 1 (2005), [arXiv:nucl-ex/0410020](#).
- [3] B. B. Back et al. (PHOBOS), *Nucl. Phys. A* **757**, 28 (2005), [arXiv:nucl-ex/0410022](#).
- [4] J. Adams et al. (STAR), *Nucl. Phys. A* **757**, 102 (2005), [arXiv:nucl-ex/0501009](#).
- [5] P. Kovtun, D. T. Son, and A. O. Starinets, *Phys. Rev. Lett.* **94**, 111601 (2005), [arXiv:hep-th/0405231](#).
- [6] J. E. Bernhard, J. S. Moreland, and S. A. Bass, *Nature Phys.* **15**, 1113 (2019).
- [7] D. Everett et al. (JETSCAPE), *Phys. Rev. C* **103**, 054904 (2021), [arXiv:2011.01430 \[hep-ph\]](#).
- [8] G. Nijs, W. van der Schee, U. Gürsoy, and R. Snellings, *Phys. Rev. C* **103**, 054909 (2021), [arXiv:2010.15134 \[nucl-th\]](#).
- [9] J. E. Parkkila, A. Onnerstad, and D. J. Kim, *Phys. Rev. C* **104**, 054904 (2021), [arXiv:2106.05019 \[hep-ph\]](#).
- [10] P. Danielewicz and M. Gyulassy, *Phys. Rev. D* **31**, 53 (1985).
- [11] P. B. Arnold, G. D. Moore, and L. G. Yaffe, *JHEP* **11**, 001 (2000), [arXiv:hep-ph/0010177](#).
- [12] P. B. Arnold, G. D. Moore, and L. G. Yaffe, *JHEP* **05**, 051 (2003), [arXiv:hep-ph/0302165](#).
- [13] J. Ghiglieri, G. D. Moore, and D. Teaney, *JHEP* **03**, 179 (2018), [arXiv:1802.09535 \[hep-ph\]](#).
- [14] J. Ghiglieri, G. D. Moore, and D. Teaney, *Phys. Rev. Lett.* **121**, 052302 (2018), [arXiv:1805.02663 \[hep-ph\]](#).
- [15] J. Noronha-Hostler, J. Noronha, and C. Greiner, *Phys. Rev. Lett.* **103**, 172302 (2009), [arXiv:0811.1571 \[nucl-th\]](#).
- [16] N. Demir and S. A. Bass, *Phys. Rev. Lett.* **102**, 172302 (2009), [arXiv:0812.2422 \[nucl-th\]](#).
- [17] S. Pal, *Phys. Lett. B* **684**, 211 (2010), [arXiv:1001.1585 \[nucl-th\]](#).

- [18] A. S. Khvorostukhin, V. D. Toneev, and D. N. Voskresensky, *Nucl. Phys. A* **845**, 106 (2010), [arXiv:1003.3531 \[nucl-th\]](#).
- [19] A. Tawfik and M. Wahba, *Annalen Phys.* **522**, 849 (2010), [arXiv:1005.3946 \[hep-ph\]](#).
- [20] P. Alba, R. Bellwied, M. Bluhm, V. Mantovani Sarti, M. Nahrgang, and C. Ratti, *Phys. Rev. C* **92**, 064910 (2015), [arXiv:1504.03262 \[hep-ph\]](#).
- [21] C. Ratti, S. Borsanyi, Z. Fodor, C. Hoelbling, S. D. Katz, S. Krieg, and K. K. Szabo (Wuppertal-Budapest), *Nucl. Phys. A* **855**, 253 (2011), [arXiv:1012.5215 \[hep-lat\]](#).
- [22] S. K. Tiwari, P. K. Srivastava, and C. P. Singh, *Phys. Rev. C* **85**, 014908 (2012), [arXiv:1111.2406 \[hep-ph\]](#).
- [23] J. Noronha-Hostler, J. Noronha, and C. Greiner, *Phys. Rev. C* **86**, 024913 (2012), [arXiv:1206.5138 \[nucl-th\]](#).
- [24] G. P. Kadam and H. Mishra, *Nucl. Phys. A* **934**, 133 (2014), [arXiv:1408.6329 \[hep-ph\]](#).
- [25] G. P. Kadam and H. Mishra, *Phys. Rev. C* **92**, 035203 (2015), [arXiv:1506.04613 \[hep-ph\]](#).
- [26] G. P. Kadam and H. Mishra, *Phys. Rev. C* **93**, 025205 (2016), [arXiv:1509.06998 \[hep-ph\]](#).
- [27] J. B. Rose, J. M. Torres-Rincon, A. Schäfer, D. R. Oliinychenko, and H. Petersen, *Phys. Rev. C* **97**, 055204 (2018), [arXiv:1709.03826 \[nucl-th\]](#).
- [28] G. Kadam and S. Pawar, *Adv. High Energy Phys.* **2019**, 6795041 (2019), [arXiv:1802.01942 \[hep-ph\]](#).
- [29] R. K. Mohapatra, H. Mishra, S. Dash, and B. K. Nandi, (2019), [arXiv:1901.07238 \[hep-ph\]](#).
- [30] M. Troyer and U.-J. Wiese, *Phys. Rev. Lett.* **94**, 170201 (2005), [arXiv:cond-mat/0408370](#).
- [31] C. Ratti, *Rept. Prog. Phys.* **81**, 084301 (2018), [arXiv:1804.07810 \[hep-lat\]](#).
- [32] T. D. Cohen, H. Lamm, S. Lawrence, and Y. Yamauchi (NuQS), *Phys. Rev. D* **104**, 094514 (2021), [arXiv:2104.02024 \[hep-lat\]](#).
- [33] I. Danhoni and G. D. Moore, *JHEP* **02**, 124 (2023), [arXiv:2212.02325 \[hep-ph\]](#).
- [34] M. I. Gorenstein, M. Hauer, and O. N. Moroz, *Phys. Rev. C* **77**, 024911 (2008), [arXiv:0708.0137 \[nucl-th\]](#).
- [35] J. Noronha-Hostler, J. Noronha, and C. Greiner, *Phys. Rev. C* **86**, 024913 (2012), [arXiv:1206.5138 \[nucl-th\]](#).
- [36] E. McLaughlin, J. Rose, T. Dore, P. Parotto, C. Ratti, and J. Noronha-Hostler, *Phys. Rev. C* **105**, 024903 (2022), [arXiv:2103.02090 \[nucl-th\]](#).
- [37] J. Hammelmann, J. Staudenmaier, and H. Elfner, (2023), [arXiv:2307.15606 \[nucl-th\]](#).

- [38] J. S. San Martin, R. Hirayama, J. Hammelmann, J. M. Kartheim, P. Parotto, J. Noronha-Hostler, C. Ratti, and H. Elfner, (2023), [arXiv:2309.01737 \[nucl-th\]](#).
- [39] S. Cremonini, *Mod. Phys. Lett. B* **25**, 1867 (2011), [arXiv:1108.0677 \[hep-th\]](#).
- [40] Y. Kats and P. Petrov, *JHEP* **01**, 044 (2009), [arXiv:0712.0743 \[hep-th\]](#).
- [41] M. Brigante, H. Liu, R. C. Myers, S. Shenker, and S. Yaida, *Phys. Rev. D* **77**, 126006 (2008), [arXiv:0712.0805 \[hep-th\]](#).
- [42] A. Buchel, R. C. Myers, and A. Sinha, *JHEP* **03**, 084 (2009), [arXiv:0812.2521 \[hep-th\]](#).
- [43] M. Brigante, H. Liu, R. C. Myers, S. Shenker, and S. Yaida, *Phys. Rev. Lett.* **100**, 191601 (2008), [arXiv:0802.3318 \[hep-th\]](#).
- [44] N. Christiansen, M. Haas, J. M. Pawłowski, and N. Strodthoff, *Phys. Rev. Lett.* **115**, 112002 (2015), [arXiv:1411.7986 \[hep-ph\]](#).
- [45] P. Lowdon, R.-A. Tripolt, J. M. Pawłowski, and D. H. Rischke, *Phys. Rev. D* **104**, 065010 (2021), [arXiv:2104.13413 \[hep-th\]](#).
- [46] X. An et al., *Nucl. Phys. A* **1017**, 122343 (2022), [arXiv:2108.13867 \[nucl-th\]](#).
- [47] V. Dexheimer, J. Noronha, J. Noronha-Hostler, C. Ratti, and N. Yunes, *J. Phys. G* **48**, 073001 (2021), [arXiv:2010.08834 \[nucl-th\]](#).
- [48] A. Lovato et al., (2022), [arXiv:2211.02224 \[nucl-th\]](#).
- [49] A. Sorensen et al., *Prog. Part. Nucl. Phys.* **134**, 104080 (2024), [arXiv:2301.13253 \[nucl-th\]](#).
- [50] O. Soloveva, D. Fuseau, J. Aichelin, and E. Bratkovskaya, *Phys. Rev. C* **103**, 054901 (2021), [arXiv:2011.03505 \[nucl-th\]](#).
- [51] G. S. Denicol, C. Gale, S. Jeon, and J. Noronha, *Phys. Rev. C* **88**, 064901 (2013), [arXiv:1308.1923 \[nucl-th\]](#).
- [52] J. Grefa, M. Hippert, J. Noronha, J. Noronha-Hostler, I. Portillo, C. Ratti, and R. Rougemont, *Phys. Rev. D* **106**, 034024 (2022), [arXiv:2203.00139 \[nucl-th\]](#).
- [53] J. Auvinen, J. E. Bernhard, S. A. Bass, and I. Karpenko, *Phys. Rev. C* **97**, 044905 (2018), [arXiv:1706.03666 \[hep-ph\]](#).
- [54] C. Shen, B. Schenke, and W. Zhao, *Phys. Rev. Lett.* **132**, 072301 (2024), [arXiv:2310.10787 \[nucl-th\]](#).
- [55] A. Monnai, S. Mukherjee, and Y. Yin, *Phys. Rev. C* **95**, 034902 (2017), [arXiv:1606.00771 \[nucl-th\]](#).

- [56] A. Monnai, B. Schenke, and C. Shen, *Int. J. Mod. Phys. A* **36**, 2130007 (2021), [arXiv:2101.11591 \[nucl-th\]](#).
- [57] P. Carzon, M. Martinez, M. D. Sievert, D. E. Wertepny, and J. Noronha-Hostler, *Phys. Rev. C* **105**, 034908 (2022), [arXiv:1911.12454 \[nucl-th\]](#).
- [58] C. Plumberg *et al.*, in 30th International Conference on Ultrarelativistic Nucleus-Nucleus Collisions (2023) [arXiv:2312.07415 \[hep-ph\]](#).
- [59] C. Plumberg *et al.*, (2024), [arXiv:2405.09648 \[nucl-th\]](#).
- [60] R. Venugopalan and M. Prakash, *Nucl. Phys. A* **546**, 718 (1992).
- [61] M. Albright, J. Kapusta, and C. Young, *Phys. Rev. C* **90**, 024915 (2014), [arXiv:1404.7540 \[nucl-th\]](#).
- [62] V. Vovchenko and H. Stoecker, *Comput. Phys. Commun.* **244**, 295 (2019), [arXiv:1901.05249 \[nucl-th\]](#).
- [63] E. LIFSHITZ and L. PITAEVSKI, in Physical Kinetics, Course of Theoretical Physics, Vol. 10, edited by E. LIFSHITZ and L. PITAEVSKI (Pergamon, Amsterdam, 1981) pp. 1–88.
- [64] V. Vovchenko, D. V. Anchishkin, and M. I. Gorenstein, *Phys. Rev. C* **91**, 024905 (2015), [arXiv:1412.5478 \[nucl-th\]](#).
- [65] S. Borsanyi, G. Endrodi, Z. Fodor, C. Hoelbling, S. Katz, S. Krieg, C. Ratti, and K. K. Szabo (Wuppertal-Budapest), *J. Phys. Conf. Ser.* **316**, 012020 (2011), [arXiv:1109.5032 \[hep-lat\]](#).
- [66] R. Bellwied, S. Borsanyi, Z. Fodor, J. Günther, S. D. Katz, C. Ratti, and K. K. Szabo, *Phys. Lett. B* **751**, 559 (2015), [arXiv:1507.07510 \[hep-lat\]](#).
- [67] S. Borsanyi, Z. Fodor, J. N. Guenther, R. Kara, S. D. Katz, P. Parotto, A. Pasztor, C. Ratti, and K. K. Szabo, *Phys. Rev. Lett.* **125**, 052001 (2020), [arXiv:2002.02821 \[hep-lat\]](#).
- [68] A. Bazavov *et al.* (HotQCD), *Phys. Lett. B* **795**, 15 (2019), [arXiv:1812.08235 \[hep-lat\]](#).
- [69] H. T. Ding, O. Kaczmarek, F. Karsch, P. Petreczky, M. Sarkar, C. Schmidt, and S. Sharma, (2024), [arXiv:2403.09390 \[hep-lat\]](#).
- [70] R. Rougemont, R. Critelli, J. Noronha-Hostler, J. Noronha, and C. Ratti, *Phys. Rev. D* **96**, 014032 (2017), [arXiv:1704.05558 \[hep-ph\]](#).
- [71] N. Su, *Commun. Theor. Phys.* **57**, 409 (2012), [arXiv:1204.0260 \[hep-ph\]](#).
- [72] S. Mogliacci, J. O. Andersen, M. Strickland, N. Su, and A. Vuorinen, *JHEP* **12**, 055 (2013), [arXiv:1307.8098 \[hep-ph\]](#).

- [73] N. Haque, A. Bandyopadhyay, J. O. Andersen, M. G. Mustafa, M. Strickland, and N. Su, *JHEP* **05**, 027 (2014), [arXiv:1402.6907 \[hep-ph\]](#).
- [74] E. Braaten, *Phys. Rev. Lett.* **74**, 2164 (1995), [arXiv:hep-ph/9409434](#).
- [75] E. Braaten and A. Nieto, *Phys. Rev. D* **51**, 6990 (1995), [arXiv:hep-ph/9501375](#).
- [76] E. Braaten and A. Nieto, *Phys. Rev. D* **53**, 3421 (1996), [arXiv:hep-ph/9510408](#).
- [77] K. Kajantie, M. Laine, K. Rummukainen, and M. E. Shaposhnikov, *Nucl. Phys. B* **458**, 90 (1996), [arXiv:hep-ph/9508379](#).
- [78] K. Kajantie, M. Laine, K. Rummukainen, and M. E. Shaposhnikov, *Nucl. Phys. B* **503**, 357 (1997), [arXiv:hep-ph/9704416](#).
- [79] F. S. Bemfica, M. M. Disconzi, V. Hoang, J. Noronha, and M. Radosz, *Phys. Rev. Lett.* **126**, 222301 (2021), [arXiv:2005.11632 \[hep-th\]](#).
- [80] D. Almaalol, T. Dore, and J. Noronha-Hostler, (2022), [arXiv:2209.11210 \[hep-th\]](#).
- [81] H. B. Callen and T. A. Welton, *Phys. Rev.* **83**, 34 (1951).
- [82] R. Kubo, *J. Phys. Soc. Jap.* **12**, 570 (1957).
- [83] T. Dore, J. Noronha-Hostler, and E. McLaughlin, *Phys. Rev. D* **102**, 074017 (2020), [arXiv:2007.15083 \[nucl-th\]](#).
- [84] T. Dore, J. M. Karthein, I. Long, D. Mroczek, J. Noronha-Hostler, P. Parotto, C. Ratti, and Y. Yamauchi, *Phys. Rev. D* **106**, 094024 (2022), [arXiv:2207.04086 \[nucl-th\]](#).
- [85] C. Chattopadhyay, U. Heinz, and T. Schaefer, *Phys. Rev. C* **107**, 044905 (2023), [arXiv:2209.10483 \[hep-ph\]](#).
- [86] A. Onuki, *Phys. Rev. E* **55**, 403 (1997).
- [87] G. D. Moore and O. Saremi, *JHEP* **09**, 015 (2008), [arXiv:0805.4201 \[hep-ph\]](#).
- [88] M. Martinez, T. Schäfer, and V. Skokov, *Phys. Rev. D* **100**, 074017 (2019), [arXiv:1906.11306 \[hep-ph\]](#).